

Observed internal tides and near-inertial waves on the continental shelf and slope off Jaigarh, central west coast of India

Subeesh M. P*, Unnikrishnan A. S

CSIR-National Institute of Oceanography, Dona Paula, Goa, India, 403004.

Abstract

The characteristics of internal tides (IT) and near-inertial waves (NIW) on the continental shelf and slope off Jaigarh (17°N), central west coast of India were studied. 8-month (March-October) long Acoustic Doppler Current Profiler (ADCP) measurements made in the year 2008 were used in the present study. Analysis of sea surface heights from satellite altimeter data, where the tracks of the satellites are oriented nearly in the direction of the semimajor axis of barotropic tides, reveals the presence of diurnal and semidiurnal internal tides with surface amplitudes of about 2 cm. Baroclinic current spectra of horizontal velocities show peaks in IT frequencies of M_2 , S_2 , K_1 and O_1 and in inertial frequency (f). The observed current spectra show higher energies than those in Garrett-Munk reference spectra by about 2-3 times. Based on the estimates of "critical topography" (where the topographic slope is equal to the slope of IT) and computed barotropic body force (Baines, 1982), the shelf-edge, mid-slope and deep part of the slope region are found to be the possible generation sites of internal tides in the region. Over the period of observation, the IT on the slope are found to be energetic, with a strong IT during March to mid-April (pre-monsoon period). Whereas, on the shelf, IT are weak during the pre-monsoon and found to be strong in the southwest monsoon. The available hydrographic data and model simulated hydrography suggest that this difference is linked with the stratification changes on the shelf and slope during these seasons, where the stratification is found to be weak on the shelf and strong on the slope during pre-monsoon. Strong

*

Email address: subeeshoceanography@gmail.com (Subeesh M. P)

low-mode NIW are observed on the shelf associated with the storm events while the NIW are found to be less energetic on the slope.

Keywords:

Internal tides, Near-inertial waves, Continental slope, Eastern Arabian sea, ADCP

1. Introduction

In a stratified fluid, the vertical displacement of a fluid parcel caused by a disturbance results in its oscillation around the equilibrium position and the disturbance propagates as internal waves. Internal waves have frequencies ranging from the buoyancy frequency ($N = (g/\rho_0)\delta\rho/\delta z$; where ρ is the density and g is the acceleration due to gravity) to Coriolis frequency ($f = 2\omega\sin\phi$; where ϕ is the latitude and ω is the angular frequency of rotation of the earth). The internal waves occurring in tidal frequencies are called internal tides (IT), and those occurring in near-inertial frequency are called Near-inertial waves (NIW). When barotropic tide propagates over topographic features like ridges, slope, sills, etc., it perturbs density stratification and generates oscillations in density layers leading to the generation of internal pressure gradient and thereby internal tides (Garrett and Kunze, 2007). NIWs are mostly generated in the mixed layer by wind forcing (Alford, 2003; D'Asaro, 1985). Oscillations of internal waves are baroclinic in nature and are associated with strong vertical shear, which leads to instability and turbulence in water column (Garrett and Kunze, 2007). Breaking of IT and NIW are an important energy source for mixing in the deep and shallow ocean (Lamb, 2014; Munk and Wunsch, 1998).

A significant fraction of the internal tides on the shelf-slope region is generated by the oscillating barotropic tide across the shelf-slope (Colosi et al., 2001; Duda et al., 2004). Part of the internal tide can also be generated far from the slope and shoal on to the slope and shelf (Kelly and Nash, 2010; Nash et al., 2004). Once generated, the low-mode internal tides can travel far from the source without energy dissipation until they reach shallow water. On the slope, the observed IT contains both locally and remotely generated IT. Moreover, IT interacts with background currents and mesoscale eddies, whose speeds are comparable to those of the IT, resulting in the Doppler shifting (Gerkema et al., 2013) and refraction of IT. All these processes can make IT incoherent with the local barotropic forcing, such that the observed

IT on the shelf and slope regions need not necessarily be coherent with the barotropic tides of the region.

We used the data obtained from Acoustic Doppler Current Profilers (ADCP) moored on the continental shelf and slope off Jaigarh (Fig. 1) to describe the internal waves in the region. The mooring locations lie in latitudes (17°N) lower than the critical latitudes for both semidiurnal (75°N) and diurnal (30°N) internal tides so that in this region IT can propagate as free waves at both frequencies. In an earlier paper (Subeesh et al., 2013), we discussed the characteristics of internal tides at several locations on the continental shelf off the west coast including Jaigarh. The present paper mainly focuses on the IT characteristics on the slope region and variations over the slope to shelf region are also described. The continental shelf in the southern part of the Indian west coast is narrow (about 85 km at 9°N) which broadens gradually towards the north, reaching about 140 km at Jaigarh (17°N). The central west coast of India is characterized by the presence of large semidiurnal tides (Unnikrishnan et al., 1999). The wide continental shelf in the northern part is believed to generate strong barotropic tides and thereby expected to be one of the strong generation sites for baroclinic tides. Oceanography off the Indian west coast varies in two seasons; southwest (SW) monsoon (May-September), north-east (NE) monsoon (November-February). The ADCP data used in the present study covers three periods, the pre-monsoon (March-April), SW monsoon, and first 20 days in October (October is the transition period between SW monsoon and NE monsoon). The west coast experiences low-frequency seasonally reversing coastal current, known as the West India Coastal Current (WICC). The WICC flows equatorward during SW monsoon and reverses and flows poleward during NE monsoon (Shetye et al., 1991, 1990). Another characteristic feature is the occurrence of seasonal upwelling off this coast during SW monsoon (Rao et al., 2008; Shankar et al., 2005; Shenoi et al., 2005).

The study of internal waves on the shelf and slope regions off the west coast of India was so far limited due to the non-availability of current observations. The earlier studies were carried out using the short records of current meter (Shenoi et al., 1988) and temperature data (Kumar et al., 2010; Unnikrishnan and Antony, 1990). These studies were limited to shelf and nearshore regions. Shankar et al. (2005) reported the presence of internal tides in the deep location off Jaigarh and Goa (15°N) using continuous CTD measurements. Harmonic analysis of temperature time series off Goa showed significant isothermal fluctuations in tidal frequencies of M_2 , S_2 and

O_1 (amplitudes of 0.5°C , 0.45°C and 0.35°C respectively at 100 m depth). The absence of continuous long-term current and hydrographic measurements restricted further detailed studies of IT on the slope. The paucity of current measurements has been overcome with the data collected during the several cruises conducted by CSIR-NIO by deploying a set of ADCPs at about 100 m and 1000 m respectively on the shelf and slope at several locations off the west and east coast of India. For the present study, we used data from one of the mooring pairs located on the shelf and slope off Jaigarh, central west coast of India. In our earlier study, the data from ADCP moorings on the shelf off the west coast of India were analysed to describe the variability and structure of internal tides (Subeesh et al., 2013). At all the shelf locations, the M_2 IT are found to be the strongest followed by K_1 and S_2 with a dominant first mode vertical structure. The shelf region off Jaigarh is particularly significant from an IT point of view due to the presence of large amplitudes of M_2 , S_2 , K_1 and O_1 , where all four major tidal constituents have significant amplitudes and a prominent spring-neap cycle is found. Moreover, the ellipses of all major tidal constituents are aligned in a cross-shore direction. Off Jaigarh, M_2 barotropic tidal currents are about three times larger than those off Goa (15°N). It is found that the variations in seasonal stratification strongly influence the IT on the shelf region; especially IT are found to be weak during pre-monsoon when the stratification is weak, and it is strong during SW monsoon when the stratification increases (Subeesh et al., 2013). Baines (1982) estimated the internal tidal energy fluxes of semidiurnal components (M_2 , S_2) at different continental shelf-slope regions of the world, including the northern part of the shelf off western India (Porbandar-Goa, 21° - 16°N), and showed large conversion of barotropic to baroclinic energy taking place in the region. Their study showed that the regions having wide continental shelves make a substantial contribution to the global internal tidal energy flux. In this context, we analysed the data off Jaigarh to describe the IT characteristics in detail.

The paper is organized as follows: Section 2 describes the study area and the methodology used. Section 3 describes IT in the region observed by satellite altimetry. Section 4 provides a detailed description of the seasonal variations in stratification in the region and associated changes in the IT modal structure. Section 5 provides the description of IT using ADCP data. Section 6 discusses the possible causes of generation of IT in terms of criticality parameter and barotropic forcing in the region. Section 7 deals with the near-inertial waves (NIW). Section 8 summarizes and concludes the

study.

2. Data and Methods

The upward looking 75 Khz RDI ADCP mooring was deployed at about 438 m of water depth on the slope off Jaigarh (17.2°N and 71.5°E) (Fig. 1) on 03rd March 2008, and it was recovered on 20th October of the same year. Water depth of the location is about 1100 m. Measurements were made at an interval of 1 hour in time and 8 m in vertical. The ADCP data analyzed in this study ranged between 55 m to 438 m depths, as the measurements over the upper 55 m depth were removed due to contamination of data. The accuracy of the velocity measurements is better than 1.55 cm s^{-1} (Amol et al., 2012). We also used ADCP measurements (described in Subeesh et al., 2013) on the shelf off Jaigarh (Fig. 1) to describe the shelf-slope variation of IT and to study the NIW. The U and V components of the measured velocity vectors were rotated with respect to the orientation of isobath (about 44° with respect to the true north) to get the cross and along-isobath components of velocities.

Strictly, separation of barotropic and baroclinic currents on the slope is not possible since the data were available only up to the upper half of the water column. However, we considered the vertically averaged current in the available water column as barotropic current at the mooring location. Harmonic analysis was performed for this vertically averaged current to obtain the barotropic tidal current (BT). We also extracted BT from 1/12 degree OTIS (Oregon State University Tidal Inversion Software, version 7.2) regional tidal solution for the Indian Ocean (Egbert and Erofeeva, 2002) and found an agreement between the two which allowed us to consider vertically averaged currents as BT with a good level of confidence. The difference between observed and barotropic current was taken as baroclinic currents. Baroclinic currents were subjected to harmonic analysis to obtain baroclinic tidal currents. Baroclinic currents were analysed for the period of three months March-May, June-August and a period covering September and October. Harmonic analysis, using TASK-2000 software (Bell et al., 1999), was done for the baroclinic currents separately for these three periods, and tidal ellipses were constructed. Besides, a third order band pass filter was used to separate semidiurnal (1.8-2.2 cpd) and diurnal (0.8-1.2 cpd) internal tides from baroclinic currents. Currents over near-inertial frequencies were derived

by a third order filtering ($0.85-1.15f$, where f is the local inertial frequency) of observed horizontal currents (Chen et al., 2013).

3. Surface signatures of IT from satellite altimetry

Before going into the detailed analysis of the ADCP data, we show the presence of M_2 and K_1 internal tides in the region as observed in satellite altimeter data. The aim of this section is to describe the broad characteristics of internal tides on the slope and deep regions (water depth >500 m) off the west coast of India. Satellite altimeter measures sea-surface height (SSH) along its path in a regular interval with an accuracy of about 2 cm. However, if there are sufficient number of measurements, altimetry can resolve tidal signals with 1-2 mm accuracy (Zhao et al., 2012). Even if the internal tides are confined to the interior part of the sea, IT leaves small signatures on the sea surface that can be found in the altimeter measurements (Maraldi et al., 2011; Merrifield et al., 2001; Ray and Cartwright, 2001). Harmonic analysis of the sea-level time series gives the amplitude of each constituent that is a combination of both barotropic and phase-locked baroclinic tide. Application of a high-pass filter (<1000 km) in the space domain will remove the long-wavelength barotropic tide leaving out the IT signals (Zhao et al., 2012). Fig. 1 shows that the two ascending tracks of the satellites nearly cross the shelf break at right angles. The barotropic ellipses on the shelf in this region are also oriented nearly perpendicular to the shelf (Fig. 1) so that we can expect the altimeter to capture the internal tide signal. One of the tracks stands for the TOPEX/Poseidon (T/P) satellite, which started in 1992 and shifted to the next orbit (interleaved orbit) in 2002. Further measurements were maintained by the next two satellites Jason-1 (J1) (2002-2009) and Jason-2 (J2) (2008-till now) along the same track. The other track is called interleaved track that is the track of shifted T/P after the starting of J1. J1 was also shifted to the same orbit after the arrival of J2. The derived constituents from combined altimetry records of T/P-J1-J2 and T/PN-J1N (interleaved track) are available in the AVISO website (www.aviso.org). The time period considered for the harmonic analysis is 23-Nov-1993 to 19-May-2011 (T/P-J1-J2) and 20-Sep-2002 to 14-May-2011 (T/PN-J1N) which consist of 17.4 years and 8.6 years respectively. The repeat period of satellites is 9.9156 days. The time series of both combined missions is enough to resolve major tidal constituents (M_2 , S_2 , K_1 and O_1). We used a high pass filter (<1000 km) in space to remove the barotropic part from the satellite-derived tide.

Satellite measurements over the shallow region (water depth <500 m) were discarded from the analysis. We also used a global tidal model, FES 2012 (Carrère et al., 2012), to remove the barotropic signal from the total tide. The amplitude of barotropic tide for each constituent, M_2 and K_1 , at every satellite measurement point was extracted from the model output and subtracted from the total signal. Fig. 2 shows the along track amplitudes of M_2 and K_1 internal tide obtained from the above two methods. The pattern of outputs from both methods visibly matches well. The RMS error between the two methods lies in 2-6 mm. Fig. 2 shows oscillation of M_2 and K_1 internal tides along the two tracks. Towards the shelf region, the amplitude of oscillation is found to be high and it reduces towards the deep water. This is true in both tracks. This suggests that the shelf-slope region off Jaigarh could be a possible generation site of internal tides, with IT propagating away from the region of generation. Spectral analysis of the M_2 and K_1 IT reveals peaks at wavelengths near about 125 km and 270 km (Figs. 2f and g) respectively. The M_2 peak is more clearly visible in T/PN-J1N track than that in T/P-J1-J2 track. Theoretical wavelengths of M_2 and K_1 in the deep ocean were calculated from the phase-speed of the first mode baroclinic wave, which is about 2.4 m/s (Chelton et al., 1998). The wave lengths of M_2 and K_1 for these values are 112 km and 250 km respectively. The spectral peaks occur close to the theoretical values. Spectral energy mainly peaks at first mode IT and higher mode peaks are relatively small.

4. Ocean Stratification

In this section, we describe the hydrographic observations at a location close to the slope mooring location. Fig. 3 shows the CTD observations from three cruises, which were carried out in February, April and June. The CTD measurements during February and April were taken in the same year as that of ADCP observations while measurements in June were taken in 2002. The available hydrographic data cover three seasons. (1) February represents winter, (2) April falls in the pre-monsoon and (3) June represents SW monsoon period. In February, the mixed layer depth is found to be shallow (15 m) even in the presence of 30 m isothermal depth. In February, salinity values are found to be low (about 34.7) in the surface layers as compared to those in other months (35.8 and 36 in April and June respectively). The plausible reason for salinity decrease at the northern region is the advection of low saline waters from the southern region during NE monsoon by the WICC (Naqvi,

1991). The low saline waters might have a role in determining the shallow mixed layer depth in February. This indicates that salinity has an important role in the stratification of the region. During the pre-monsoon period, upper ocean layers start to warm due to the increased intensity of short-wave radiation. During the starting period of the SW monsoon (May and June), sea surface temperature becomes maximum, which decreases gradually with the progress of the SW monsoon. The mixed layer in April and July is found to be relatively deep (36 and 25 m respectively) compared to that in February. The values of buoyancy frequency (N) are almost similar in all the above three months, where the depth-averaged N is about 3 cph in all the three months.

4.1. Normal mode decomposition

In a continuously stratified ocean, internal waves can be represented by the vertical normal modes (Kundu and Cohen, 1990). For a flat bottom, the baroclinic modes for vertical displacement $\Phi(z)$ can be estimated by solving the equation (1), an eigenvalue problem, under hydrostatic, inviscid and the Boussinesq approximations.

$$\frac{d^2\Phi(z)}{dz^2} + \frac{N^2(z)}{c_n^2}\Phi(z) = 0 \quad (1)$$

For the horizontal velocity, the equation is,

$$\Pi(z) = \rho_0 c_n^2 \frac{d\Phi(z)}{dz} \quad (2)$$

Where $\Phi(z)$ is the eigenfunction, c_n is the eigenvalue for n^{th} mode, and $\rho_0 = 1028 \text{ kg/m}^3$ is the reference density. The displacement, $\Phi(z)$ depends only on the buoyancy frequency $N(z)$ and the water depth. For a constant stratification, the equation can be solved analytically. For varying stratification, the equation must be solved numerically by setting a boundary condition at the sea floor and sea surface ($\Phi(0) = \Phi(-H) = 0$ at $z = 0$, $z = -H$ respectively). All the motions are confined into these boundaries so that the waves are reflected from boundaries and propagate horizontally. $\Phi(z)$ and $\Pi(z)$ describe the modal structures for vertical and horizontal velocity of internal waves respectively. Strictly, the normal mode decomposition is valid for a flat horizontal topography for vertically standing waves. However, several studies (Klymak et al., 2011; Lee et al., 2012) show that the normal

mode decomposition is useful on the slope regions. Once a solution is obtained, the phase speed (c_p), group speed (c_g) and horizontal wavenumber (k_x) of internal tides with frequency ω can be derived from the dispersion relation as follows

$$c_p = \frac{\omega}{(\omega^2 - f^2)^{\frac{1}{2}}} c_n \quad (3)$$

$$c_g = \frac{(\omega^2 - f^2)^{\frac{1}{2}}}{\omega} c_n \quad (4)$$

$$k_x = \frac{(\omega^2 - f^2)^{\frac{1}{2}}}{c_n} \quad (5)$$

Fig. 3 shows buoyancy frequency profiles near the slope mooring and the first three baroclinic modes for vertical displacement and horizontal velocity in three representative months of different seasons. Mode-1 of the horizontal velocity has a node at 250 m; mode 2 has two nodes at 100 m and 600 m. The speed of the first mode internal wave is about 1.6-1.9 m/s on the slope. The linear first mode speed is 2.4 m/s in deep water off the slope (Chelton et al., 1998). The phase speed, group speed and the wavelength of major tidal constituents were calculated from equations 3-5 (Table 1). Though the variation of stratification is small in the three different months, the phase speed and wavelength of the internal tide for each constituent are found to vary from month to month. The largest values are found in February and the smallest in June (Fig. 3, Table 1). This reveals that even a small change in stratification influences the propagation of internal tides in the region.

4.2. Isopycnal displacement

We estimated the isopycnal displacements determined from a 9-day 2 hourly time series CTD data (Shankar et al., 2005), made in July 2002 at a deep slope location (Fig. 1) (16.94⁰N, 71.19⁰E, water depth 2250 m) about 43 km away from the slope ADCP mooring. The isopycnal displacements were calculated from the density anomaly as follows.

$$\rho'(t, z) = \rho(t, z) - \bar{\rho}(z) \quad (6)$$

Where $\bar{\rho}(z)$ is the time-mean density

$$\eta(t, z) = \rho'(t, z) \frac{\rho'}{d\rho/dz} \quad (7)$$

Where $\eta(t, z)$ is the amplitude of internal tide oscillation. The large isopycnal oscillation in diurnal and semidiurnal periods (Fig. 4) shows a significant internal tide activity in the water column. The magnitude of observed η varies between 5 m and 30 m, with maximum values found at about 100 m depth. Barotropic tidal currents for the same observation period obtained from OTIS output are also shown (Fig. 4a). Internal tides follow the barotropic tide indicating that a large fraction of internal tides in the region is phase locked with the barotropic tides. This is consistent with the previous results from the satellite altimetry (Fig. 2), where significant coherent internal tide is present in the deep region off the slope. The spectral analysis shows oscillations at tidal frequencies M_2 and K_1 and at higher frequencies (Fig. 4c).

The Garrett-Munk internal wave spectra (Equation 8) for vertical displacement (Munk, 1981) was computed as

$$F_{\zeta}(\omega) = \frac{2}{\pi} \frac{f}{N} E_0 b^2 N_0 \frac{(\omega^2 - f^2)^{1/2}}{\omega^3} \quad (8)$$

using the canonical values for $E_0 = 6.3 \times 10^{-5}$, $N_0=3$ cph and $b=1300$ m, f is the Coriolis frequency for the location. N is the local buoyancy frequency. The GM spectrum based on 2 cph buoyancy frequency is shown (Fig. 4c). Observed spectra show high energies than those in Garrett-Munk reference spectra at all the depths. The observed spectra follows ω^{-2} slope, consistent with the slope of GM spectrum.

5. Internal tides on the slope from ADCP currents

5.1. Rotary spectra of baroclinic currents

To determine the distribution of energy in different frequency bands, rotary spectra of baroclinic horizontal currents from slope ADCP mooring were computed. Rotary spectra decompose a complex velocity ($u + iv$) into clockwise and counterclockwise rotating components (Gonella, 1972). The computations were done for different depths and spectral energy obtained was averaged over the upper 50 m and the lower 50 m water columns. Spectra were computed for the entire period of observation. For the deep ocean, i.e. away from boundaries, GM spectrum represents internal wave continuum, a continuous spectrum of waves between Coriolis frequency (f) and buoyancy frequency (N). The clockwise and counterclockwise GM spectra (Levine et al., 1997) for the upper ($N=10$ cph) and lower water columns

($N=1$ cph) were computed separately. Clockwise (CW) and counterclockwise (CCW) spectra of cross-isobath component of velocity along with the smooth Garrett-Munk (GM) spectrum are shown in Figs. 5a and b. The energy of internal waves is not distributed as smoothly in the observed spectra as that in the GM spectra. Observed spectra lie above the curve of the GM spectra with multiple peaks at different frequencies. In the observed current spectra, the dominant spectral lines are located at M_2 , S_2 , N_2 , K_1 and O_1 frequencies and at Coriolis frequency (f). Another significant peak is observed at harmonics of M_2+O_1 and M_4 . The former peak arises from the non-linear interaction and advection of semidiurnal and diurnal internal tides (Xu et al., 2013). Observed spectra also show a peak at M_2+f . Alford et al. (2012) suggested that the peak at M_2+f is generally associated with the heaving of the NIW motion by the oscillation of the internal tide. The slope of current spectra is more or less consistent with the slope of GM which varies from $\omega^{-1.5}$ to ω^{-2} .

The level of energy over the NIW period is relatively low, and it is distributed in a broader band compared to those of IT frequencies, for which the energy distribution is confined to narrow bands with well-resolved peaks. Near-inertial energy is strong in the top layer of the water column which gets reduced downwards. The CCW component of near-inertial current is almost negligible (Fig. 5a), that is, polarization (ratio of CW and CCW) is maximum at NIW frequency and decreases with increasing frequency (Gonella, 1972). CW spectrum dominates CCW spectrum in internal wave spectra (Figs. 5a and b), which is found to be consistent with the internal wave theory for the northern hemisphere. We calculated the vertically averaged CW to CCW ratio, and those were compared with the theoretical ratio $(\frac{(\omega+f)^2}{(\omega-f)^2})$ for the random superposition of free linear internal waves (Lien et al., 2013; Müller et al., 1978). Theoretical ratio is found to be closer to the observed ratio for frequencies greater than tidal frequencies (Fig. 5c). However, for the tidal frequencies, the values deviate from the theoretical curve, which might be due to the nonlinearity associated with the semidiurnal and diurnal tides.

5.2. Tidal currents

We show both cross and along-isobath sub-inertial currents (Figs. 6a and b) along with the band-passed IT (Fig. 6d) on the slope off Jaigarh. Cross-isobath sub-inertial currents (Fig. 6a) are found to be weak during the entire period of observation. Cross-isobath raw currents are tidally dominant, where 64% of the total variance is explained by barotropic and baroclinic

tides. In the along-isobath direction, tidal currents account for only 13% of total variance. Barotropic tidal current obtained by the harmonic analysis of cross-isobath barotropic current for the month of March is also shown in Fig. 6c. We compared the barotropic velocity with the predictions from a global tidal model (OTIS) (Fig. 6c). The observed barotropic tidal currents show good agreement with OTIS output with an RMS error of about 1 cm s^{-1} . Thus, the method of removing barotropic signals from the total currents by vertically averaging current is found to be valid for slope location. Cross-isobath baroclinic currents were band-passed for total (0.5-6.0 cpd), semidiurnal (1.8-2.2 cpd) and diurnal (0.8-1.2 cpd) internal tides (Figs. 6d, g and h). Barotropic tidal currents show an apparent fortnightly cycle. Internal tides on the slope are strong, with the maximum speed attaining to about 32 cm s^{-1} in the upper layer of the water column. Strongest IT is always observed during the period of spring tide, indicating the coherency of internal tides with local barotropic tides. This is true in band-passed semidiurnal and diurnal IT, where they also followed the spring-neap cycle of their barotropic counterpart (not shown). Internal tides are found to be strong in the upper water column (55-100 m), where the stratification is high. Figs. 6g and 6h show a two-day time series of band-pass filtered semidiurnal and diurnal IT along with their barotropic tides (Figs. 6e and f). The currents in the upper layer are clearly out of phase with those in the lower layer. The semidiurnal IT shows low vertical mode standing wave structure (Fig. 6g). In diurnal IT, higher modes are also significant (Fig. 6j). During many other periods, the downward propagation of diurnal IT is also found to be strong with higher mode vertical structure (For instance during April and June). Figs. 6i and 6j show the vertical shear ($S = ((\partial u / \partial z)^2, (\partial v / \partial z)^2)$) computed at 8 m interval for both semidiurnal and diurnal IT. Shear depends on the vertical structure of internal tide. Semidiurnal shear is strongest at about 200 m depth, which indicates the dominance of first mode. Diurnal IT shear is found to be significant in different layers indicating multiple modal structures.

5.3. Tidal ellipses

Both barotropic and baroclinic currents were subjected to harmonic analysis and tidal ellipses were constructed. Ellipse parameters of barotropic tides are listed in Table 2. We also examined the temporal stability of barotropic tidal currents by doing the harmonic analysis for different periods. We divided barotropic currents into four periods of two months and harmonic analysis was carried out in each period. Results obtained from a full-month

harmonic analysis of barotropic currents were compared with those obtained from the two-month harmonic analyses. The difference in magnitudes from two analyses lies in the limit of 1 cm s^{-1} . Thus the seasonal variation of barotropic currents is found to be negligible. Barotropic tidal ellipses of M_2 , S_2 , K_1 and O_1 on the slope location are shown in Fig. 7. Ellipses consistently rotate in a clockwise direction and appeared more or less in the same shape with the semimajor axis oriented across the bathymetric contours. The cross-isobath barotropic M_2 tidal current (4.8 cm s^{-1}) is found to be three times stronger than that of along-isobath current (1.6 cm s^{-1}).

Baroclinic tidal ellipse parameters for every depth were calculated by harmonic analysis of baroclinic currents. To study the seasonal variation of IT, we divided baroclinic currents into two periods of three months March-May, June-August and a period consisting of September and October. Harmonic analysis was carried out for each period and the results are shown in Fig. 7. Tidal ellipses computed for the September-October period show similar patterns of those in June-August and hence not shown. Internal tides greatly vary in time by the background changes in currents and stratification. These variations cannot fully be resolved through the harmonic analysis, which gives only an average pattern of each IT constituent. The present analysis shows that M_2 , S_2 , K_1 and O_1 are the most significant constituents for the region. For M_2 , the semimajor axis is about 12 cm s^{-1} at the surface, and it gradually decreases with the depth reaching a minimum of 2 cm s^{-1} at 200 m depth. The tidal ellipses show seasonal variations with M_2 and K_1 , IT being the strongest in March-May period (semimajor axis at the upper layer is 12 cm s^{-1} and 4 cm s^{-1} respectively) when compared to June-August period (9 cm s^{-1} and 3.7 cm s^{-1} respectively). Even though magnitudes of tidal ellipses vary from season to season, their vertical structure is found to be similar throughout the period (Fig. 7). This may be due to the small variations in pycnocline depth during the observational period. The vertical structure of the ellipses (Fig. 7) shows that internal tides are dominated by first baroclinic mode motion with a minimum occurring in the middle depth. However, the vertical structure of S_2 is complex with two minima, where the second mode vertical structure seems to be dominant (Fig. 7c). All the baroclinic ellipses are oriented in the same direction as those of barotropic ellipses in both seasons indicating that internal tides are coherent with the local barotropic tides. Semimajor axes of both barotropic and baroclinic ellipses are oriented across the isobaths. For freely propagating internal tide, the ratio of semiminor to semimajor axis can be obtained as f/ω , where f is

the Coriolis frequency and ω is the frequency of the wave (Petruccio et al., 1998). The theoretical value of this ratio is found to be 0.29 and 0.56 for M_2 and K_1 respectively. The observed values (varies between 0.1 to 0.5 for M_2 and 0.2 to 0.8 for K_1) are found to be consistent with the theoretical ratios.

5.4. Vertical structure of IT

EOF analysis was done to the cross-isobath and along-isobath components of band-passed (0.5-6 cpd) baroclinic IT on the slope location. Figs. 8a, b and c show the first three spatial modes of the horizontal components (shown as red colored vectors) along with the power spectra estimated for its time function (Fig. 8d). The results show that, the first mode of cross-isobath IT explains about 65% of the total variance while the second and third modes, the variance accounts for about 11% and 4% respectively. These three modes together represent 80% of the total IT variance in the region. However, in the along-isobath component, the first mode explains 40% of total variance and the second and third mode variances are 14% and 8% respectively. First mode variability in the cross and along-isobath IT exhibits a two layer structure with zero crossing at about 200 m. To examine the kinetic energy distribution over frequencies in the first three modes, power spectra of the principal components are plotted (Fig. 8d). The semidiurnal and diurnal internal tides are dominated by the first mode. We also carried out EOF analysis of baroclinic currents for both semidiurnal and diurnal bands on the slope location (Table 3). For the semidiurnal band, first and second EOF mode of the cross-isobath component represents 77% and 10% of total semidiurnal IT variance respectively. Higher modes are found to be weak. In the along-isobath semidiurnal IT, the first mode explains 55% of the total semidiurnal variance. Second and third modes explain 14% and 7% of the variance respectively. Though the diurnal IT is dominated by first mode, higher modes are also found to be significant (Table 3). This is consistent with the shear analysis, where the shear for diurnal IT is found to be large in different layers of water column (Fig. 6j), which might be due to the presence of the higher modes.

We found that the vertical structure of first and second EOF modes resembles the corresponding baroclinic normal modes for the horizontal velocity. Using a linear regression method (Lee et al., 2012) we fitted the EOF modes to the corresponding theoretical normal modes and the regression result is plotted as black colored vectors in Figs. 8a, b and c. The normal modes were calculated by using computed buoyancy frequencies for February (Fig. 3).

The normal modes were normalized to have unit variance before doing the least square fits. The first EOF mode (both U and V components) on to the first mode of the normal mode and the regression coefficient for U and V components are plotted as black-colored vectors over the first EOF mode structure in Fig. 8a. Similarly, a best matching regression model for second and third mode U, V components are shown in Figs. 8b and c respectively. The U and V components of each EOF mode are regressed to corresponding normal modes as,

$$U_{e(k)} = \alpha_k + \beta_k U_{n(k)} \quad (9)$$

Where $k=1,2$ and 3 represent different modes; α_k and β_k are the regression constants for each mode, $U_{e(k)}$ and $U_{n(k)}$ are the corresponding EOF and normal modes. The first mode structure of U (V) shows an r^2 value of 0.97 (0.87) to the normal mode; for the second mode it reduces to 0.57 (0.72) and it further reduces to 0.1 (0.004) for the third. This suggests that the first and second mode variability of the observed currents is largely explained by the corresponding baroclinic normal mode structure. The third mode does not show any obvious relationship with its corresponding normal mode structure as seen in the Fig. 8c. We repeated the experiment for different months and found that results are nearly identical (not shown).

5.5. Seasonal and Cross-shelf Variations

In this section, we show the seasonality of IT over slope and shelf regions and slope-shelf variation of IT amplitudes. Figs. 9a and b show the band-passed barotropic and internal tide variance ($u^2 + v^2$) running averaged over three days for the shelf and slope regions respectively. Internal tide variance was also averaged over the depth. The barotropic tidal currents do not vary with seasons on both slope and shelf locations. However, internal tides show seasonality in their magnitudes. On the slope, internal tides are found to be strong during March to the first week of April, and they are less strong during June. This continues up to the third week of September, and they intensify later. This pattern is found in semidiurnal and diurnal internal tide (Fig. 9c). We used shelf ADCP data to see whether this pattern is consistent on the shelf and found that IT are weak during March and the first two weeks of April, and they slowly start picking up strength. We analyzed the evolution of buoyancy frequency (Figs. 9d and e) on the shelf and slope during the same period computed from the simulated temperature and salinity from

MOM4p1 ocean model (Chatterjee et al., 2013). The slope was stratified during the entire period of observations with minimum variability in time. However, the shelf shows significant seasonal variations in stratification, with low stratification found during March-April and high stratification observed during SW monsoon (May-September). Available CTD observations on the shelf and slope during the same year show a similar pattern, where the slope stratification does not appreciably vary from February to April, but that of the shelf does change. On the shelf (at about 100 m), in February the temperature difference between upper and bottom water column, indicative of stratification, is about $0.5\text{-}3^{\circ}\text{C}$ and it increases to about $2\text{-}4^{\circ}\text{C}$ in April. However, towards the slope (500 m, 1000 m) region, the water column is well stratified in the above two months, where the temperature difference is about 15° and 20°C respectively (Figure not shown). The well-mixed condition of shelf during the pre-monsoon could be one reason of comparatively weak IT during March and April. Other possible mechanisms that affect the IT generation on the shelf will be discussed in section 6.3. The slope stratification is strong during the entire period, and the IT retains their strength over the period of observation.

5.6. Coherent and Incoherent IT

In this section, we discuss the relative contribution of coherent and incoherent IT on the slope and shelf regions. The broadband internal tides were extracted by 6-30 hrs band pass filtering of the baroclinic currents. This band excludes the NIW and encompasses only the coherent and incoherent IT signals. Here the coherent signal implies the predictable component that can retain a constant phase and amplitude over a given time period (Nash et al., 2012), so that it can be resolved by harmonic analysis. The incoherent IT greatly varies in time so that it cannot be resolved by the harmonic fits over a given time span. Incoherent IT can be obtained by subtracting harmonic fits from the band-passed signals. The capability of harmonic analysis to resolve internal tides varies in different time windows due to the intermittency of internal tides associated with background variability such as stratification, mesoscale eddies, currents, etc., which vary in different timescales. We performed running harmonic analysis for periods ranging from 3 days to 8 months and separated the coherent and incoherent IT for each time window (Fig. 10). We examined the intermittency of internal tides and the capability of harmonic analysis to represent the internal tides for different time windows in the shelf and slope regions.

We calculated the predictive capability of a harmonic fit for each time window by using a skill score test (Murphy, 1988; Nash et al., 2012)

$$SS_T = 100\% \times \left[1 - \frac{\langle (u' - H_T(u'))^2 \rangle}{\langle u'^2 \rangle} \right] \quad (10)$$

where u' is the band-passed cross-isobath internal tide, which includes all the signals of the period from 6 to 30 hrs. H_T is the regenerated coherent IT from harmonic analysis, where T is the time window (3 days-full months) used for the analysis. The term $(u' - H_T(u'))$ gives the incoherent part of IT. After subtracting the coherent IT from the band-passed signal, all the values were squared and averaged over time and depth. The value was then divided by the averaged band-passed signal over time and depth for the same period. 100% SS_T implies that the harmonic analysis captures all the observed variance. The tests show that the capability of harmonic analysis to capture the IT over different time windows varies over the shelf-slope region significantly. For example, on the slope, harmonic analysis of 15-day window could represent 76% of IT. When the time window was increased, the capability was found decrease. 30-day window could only represent 66% and 90-day window represented 52% of total IT (Fig. 10). On the shelf off Jaigarh, the internal tides are found to be more incoherent where even 7-day harmonic fits could only represent 69% of total IT. During March, shelf IT is found to be weak in broadband IT (Fig. 9b). 30-day and 60-day running harmonic analysis show that during March-April, the coherent internal tides are weak on the shelf and dominated by the incoherent part. The well-mixed state of shelf water might have restricted the local generation of IT there. A part of shelf IT during March-April may be shoaling from the slope, where slope IT is strong during these periods. The results from harmonic analysis over the entire period of observations show that (Fig. 10) the variance of coherent internal tides is dominant on the slope region with skill score of 56% where the IT retains its amplitude and phase over a long period of time. However, on the shelf, IT variance is high in incoherent part with skill score of only 29%. The slope internal tides are comparatively more predictable than those over the shelf.

6. Possible generation sites of internal tides

6.1. Criticality

From the generation source, IT travels as a beam with a slope c to the horizontal where the slope depends upon the frequency of IT, the stratification and the latitude. The slope c , can be estimated as,

$$c = \tan(\alpha) = \left(\frac{\omega^2 - f^2}{N^2 - \omega^2} \right)^{1/2} \quad (11)$$

Where ω is the frequency of the corresponding IT (for M_2 (K_1) it is .081 cph (.04 cph)), f the Coriolis frequency (.024 cph at 17.2°N) and N is the buoyancy frequency. Baines (1986) suggested that generation of IT would be efficient if the slope of bottom topography ($\Delta H/\Delta X$) matches the characteristic slope of internal tide (c), where even weak barotropic tides can generate internal tides.

The shelf bathymetry off Jaigarh gradually changes by a few meters from the coast and reaches shelf edge after 140 km where the depth is about 100-120 m. From shelf edge to continental rise, slope of topography varies gently where 20 km from the shelf edge, the depth reaches 1000 m. The slope of the continental slope in the region varies between 1 to 4 degrees. In the deep part (3600 m), a seamount of about 800 m tall is present, where the bottom slope reaches up to 4-6 degrees. We estimated the topographic slope from the fine resolution SRTM30_PLUS (Becker et al., 2009) bathymetry with a grid resolution about 1 km, prepared by merging satellite derived and ship acoustic sounding bathymetry (<ftp://edcsgs9.cr.usgs.gov/pub/data/srtm/SRTM30>). The buoyancy frequencies across the shelf-slope were calculated from the 13 CTD observations available in April (Fig. 11a). The 13 CTD data were averaged spatially and considered as horizontally homogeneous. The criticality parameter, which is the ratio of bottom slope and characteristic slope ($\gamma = \frac{\Delta H}{\Delta X}/c$), across the shelf-slope was also calculated (Fig. 11b). Towards the shelf edge, at 100-180 m, the bottom buoyancy frequency is about 8-10 cph. The high buoyancy frequency observed at the bottom is because the pycnocline is found near the shelf edge where the stratification is highest. The characteristic slope of M_2 IT for these values is 0.009-0.006. For K_1 , the characteristic slope will be nearly half of that of M_2 . Near shelf edge, the water depth varies 1-10 m over a horizontal distance of 1 km. The average topographic slope value is found to be 0.004. There are several critical regions, where the bottom slope matches the characteristic slope of both M_2

and K_1 frequencies (Fig. 11b). From 200 m to deeper depths, buoyancy values range between 1-3 cph. The value of the characteristic slope is reduced by a factor of ten for these frequencies. However, due to the large topographic slopes, the continental slope is found to be critical for semidiurnal and diurnal frequencies. At the mooring point, the topographic slope is about 0.04. We also estimated the criticality parameter by using the buoyancy frequency information from the MOM4p1 ocean model simulation and found that the mooring location is near critical for M_2 and K_1 , where the ratio between bottom slope and characteristic slope for M_2 is about 0.9, and that of K_1 is about 2 respectively. Bottom intensification and upward energy propagation are expected in the region. However, this cannot be substantiated in this work as we do not have the information of bottom velocity. The deep part of the slope (about 2800-3200 m) is also found to be near critical at both frequencies (not shown in Fig. 11).

6.2. Baines forcing

Baines (1982) barotropic forcing term is often used to identify the regions of internal tide generation (Da Silva et al., 2009; Merrifield and Holloway, 2002).

$$F = zN^2(z) \int Q dt \Delta(1/h) \quad (12)$$

where N represents buoyancy frequency. $Q = (uh, vh)$, Q is the barotropic mass flux vector, u and v are the velocities of zonal and meridional components of barotropic tidal-currents, and h is the water depth. $\Delta(1/h) = (dx/dh, dy/dh)$ are the topographic slopes in zonal and meridional directions respectively. The semidiurnal and diurnal barotropic mass fluxes were obtained from 1/12 degree OTIS (Oregon State University Tidal Inversion Software, version 7.2) regional tidal solution for the Indian Ocean. The fluxes for 15 days including a spring-neap cycle were interpolated to SRTM30_PLUS bathymetry, and slope of topography was determined at every grid points. Buoyancy frequency was computed using temperature and salinity monthly mean climatology (<http://www.esrl.noaa.gov/psd/data/gridded/data.godas.html>). The buoyancy values were averaged out spatially (between 69.8°-74.7°E and 13.8°-18.2°N) and considered as horizontally homogeneous. Spatially averaged buoyancy frequency matches well with the monthly mean climatology and CTD observations near the slope gave confidence us to use the spatially averaged buoyancy frequency for the calculation (Fig. 12b). The body force

was calculated at every grid point using stratification for each month. The maximum absolute value of depth-integrated body force for both semidiurnal and diurnal frequencies are shown in the Figs. 12a and b. Fig. 12 shows that the body force is strong along the shelf break (near 200 m), and it enhances towards the north. The average value of semidiurnal (diurnal) body force on the shelf break off Jaigarh is about $1 \text{ m}^2 \text{ s}^{-2}$ ($0.59 \text{ m}^2 \text{ s}^{-2}$) in January, and it increases to about $1.2 \text{ m}^2 \text{ s}^{-2}$ ($0.66 \text{ m}^2 \text{ s}^{-2}$) in June. Seasonal variation of the body force is attributed to the increase in stratification during SW monsoon. The northward intensification of body force is mainly attributed to the increase in velocity of both semidiurnal and diurnal tidal currents towards north (Figs. 12a and b). On the shelf-slope region off Jaigarh, barotropic velocities are found to be large compared to those in the southern part of the coast. The variation in the topographic slope in cross-shore direction was also noticed from the south to northern region, where the topographic gradient is found to be high in the study region and north of it. This also enhances the body force in the northern regions. The body force values on the shelf off Jaigarh are comparable to the values for other known major hotspots in the world's oceans like southern and central Bay of Biscay (Azevedo et al., 2006; Muacho et al., 2014), west Iberian coast (Magalhaes and da Silva, 2012) and Hawaiian Ridge (Merrifield and Holloway, 2002). Further north, in 19°N , the body force values are found to be significantly higher (For instance $3 \text{ m}^2 \text{ s}^{-2}$ and $2.8 \text{ m}^2 \text{ s}^{-2}$ for semidiurnal and diurnal body force respectively) than that on the shelf off Jaigarh.

6.3. Bottom intensification of IT on the shelf

In the sections 6.1 and 6.2, we discussed the possible generation sites of internal tides based on criticality and barotropic body forcing on the continental slope region off Jaigarh. In this section, we analyze the role of stratification and the topography slope in the generation of internal tides on the shelf region. In generation sites, the topography slope is expected to be comparable with the characteristic slope of internal tidal frequency. We also expect the high bottom velocities, strong vertical shear in the bottom and upward energy propagation in the generation sites. The shelf ADCP covered almost the entire water column that enabled us to study the bottom variation of internal tides in different periods of stratification. Most of the time, internal tides show low mode vertical standing wave structure. However, in June, July, and August, the internal tidal energy is found to be high in the bottom water column in both semidiurnal and diurnal frequencies.

The characteristic slope of semidiurnal and diurnal IT was calculated from the equation (11) based on the buoyancy frequency at bottom obtained from the MOM4p1 model output of temperature and salinity, and the ratio of bottom slope and the characteristic slope was estimated (Fig. 13a). Fig. 13 shows the band-passed semidiurnal and diurnal IT in July, one of the above months, along with its barotropic tidal currents. Internal tides do not follow the spring-neap cycle of the barotropic tide in July. During one neap tidal phase, (July 11-12) a strong internal tide event is observed. In diurnal also, the maximum internal tide event do not coincide with the barotropic spring time. Towards 26 to 29 July, semidiurnal IT shows bottom intensification with clear upward energy propagation. This can also be seen in diurnal IT during July 12-17. The internal tides during these periods are zoomed in Figs. 13e and 13g along with its shear evolution (Figs. 13f and h). The shear is also found to be strong in bottom layers during these periods. The shelf ADCP mooring was located in the region where the bottom topography is nearly flat. The depth variation near the mooring location is about 7 m over one-kilometer distance. The slope of the topography is thereby about 0.007. There are several events, in which the topographic slope is comparable to the characteristic slope (Fig. 13a). The bottom stratification is found to be maximum during July (Fig. 9). Due to the high stratification, the mooring location turns to be a favorable site for the internal tide generation. Strong shear at bottom and the upward energy propagation confirm this hypothesis. Though barotropic tides are weak in the diurnal compared to the semidiurnal band, internal tides are found to be stronger in diurnal frequency. This suggests that the topography is more favorable for the generation of diurnal IT for the given bottom stratification.

7. Near-inertial Waves

In this section, we describe the characteristics of NIW on the slope and the shelf regions off Jaigarh. As a first step, baroclinic currents were band-passed for 0.85-1.15 f band, and the NIW signals were extracted for both shelf and slope locations. Since the information of slope currents in upper water column (up to 50 m) is missing due to the contamination of ADCP data, we can only study those NIWs, which have penetrated from the mixed layer into the thermocline. However, the shelf ADCP covered almost the entire water column, except the near surface (12 m depth). Wind stress was calculated from the 4-day high passed QuikSCAT daily winds (Figs. 14a and

b). To show the energy distribution of NIWs over the period of observation, we performed a wavelet analysis of baroclinic currents, which provides the temporal distribution of energy in the frequency domain. The wavelet power was then averaged over the NIW band ($0.85\text{-}1.15f$) at each depth level and plotted as depth-time series (Figs. 14c and d).

7.1. NIW on the slope

On the slope, a strong NIW event is observed from April 21 to May 3 and another event is observed shortly after 3rd May which ended on May 15. The wavelet power shows that the energy maximum is present near 100 m depth. Towards the upper layers, energy is found to be weak. Fig. 14e shows a clear downward energy propagation (upward phase propagation) which indicates the possibility of remote generation of NIW. One more feature of NIW during this period is that the frequency of NIW is shifted to below the local inertial frequency where NIW peak is observed at $0.91f$. It is not observed in any other NIW events. The effective frequency of NIW is $f_e = f + \zeta_g$ where ζ_g is the relative vorticity of background geostrophic currents (Kunze, 1985). Cyclonic background current (positive vorticity) can cause the blue shift of the NIW, and anti-cyclonic (negative vorticity) flow can cause the red shift. The daily geostrophic currents were calculated from the altimeter sea level (<http://www.aviso.oceanobs.com/en/data.html>). Cyclonic and anticyclonic eddies are found to be common in the central Arabian Sea during the observational period. Vorticity ($\zeta = \partial v / \partial x - \partial u / \partial y$) was estimated from the geostrophic velocities. The vorticity is found to be negative (roughly about $-3.01 \times 10^{-6} \text{ s}^{-1}$) in the mooring location during April. The negative vorticity at the observation site might be the reason for observed frequency shifting of NIW. The estimated f_e is $0.96f$ from the above value.

7.2. NIW on the shelf

There are three main NIW events observed on the shelf, during 10-24 April, 14-23 July and 13-24 September. The decay time scale is more than a week for all the events. During all these three events, NIW shows a vertical standing wave structure (Fig. 14f) most of the time. The vertical modal structure of NIW was determined by an EOF analysis, carried out on the band-passed ($0.85\text{-}1.15f$) NIW for three events separately. For all the events, the first mode EOF is dominant with a two-layer structure, where zero crossings are found at 40-50 m depth. In April, 78% (12%) of total variance is

explained by the first mode (second mode). From September 13-24, the first mode EOF shows a clear two-layer structure and after that the higher modes become important. The second EOF mode shows three-layer structure from September 26-October 3. Shear ($S = ((\partial u / \partial z)^2, (\partial v / \partial z)^2)$) structure is consistent with the vertical structure of NIW, where most of the time shear is concentrated near zero-crossing depth (Fig. 14h). At the time when the higher modes become important, shear is found to be concentrated at corresponding zero-crossing depths. For instance, on September 13-24, when the first mode vertical structure is dominant, the maximum shear is seen near 45 m. After 24th September, shear occurs at 40 m, 60 m and 70 m depth. This is due to the presence of higher mode vertical structure of NIW during the period.

The wind effect on NIW was studied by using the QuikSCAT daily wind data with a spatial resolution of 0.25° (<http://www.ifremer.fr/cersat/en/data/download>). The wind forcing is critical to the generation of NIW (D'Asaro, 1985; Mukherjee et al., 2013). The wind pattern is similar in both shelf and slope regions. Several depressions are observed during the period of observations. No cyclone was reported in the year of 2008 in the Arabian Sea. As expected, the NIW is found to be associated with the strong wind events. However, NIW in the month of April is found to be strong (about $7-10 \text{ cm s}^{-1}$) when the wind stress is found to be weak. We calculated the wind stress from another available wind product (ECMWF, European Centre for Medium Range Weather Forecasting) and found identical results. One possible reason is that the above coarse resolution wind products may not capture some short wind burst events that cause the generation of NIW. However, this statement is not conclusive and numerical modelling studies are needed to understand the generation and propagation of NIW on the slope and shelf off Jaigarh.

8. Summary and Conclusion

In this study, we report for the first time, the presence of strong internal tides on the continental slope off the central west coast of India, using observations from satellite altimeters and ADCP current measurements. Strong internal tides are observed on the continental slope off Jaigarh (17.2° N), where they are highly coherent with the barotropic tides. On the shelf, internal tides are found to be less coherent with their barotropic counterparts. Observed near-inertial waves are found to be comparatively weak on the slope and strong on the shelf. As the NIO is well known for its strong seasonal vari-

ability associated with the NE/SW monsoon, seasonal variations of observed IT are discussed in relation to the changes in ocean stratification.

The satellite altimeter data captured the surface signature of coherent internal tide present on the shelf-slope region. Time series of computed density, at the deeper part of the continental slope (depth 2250 m) also revealed the presence of strong coherent internal tides, where the pycnocline oscillation is in phase with the barotropic tides. The presence of internal tides is more clearly visible along the T/PN-J1N track (interleaved track) than that in T/P-J1-J2 track. The T/PN-J1N track is oriented northward of the shelf where the barotropic tidal currents are found to be stronger than that on the southern shelf (Fig. 12). Moreover, the T/PN-J1N track is aligned more perpendicular to the shelf, in the same direction of semimajor axis of M_2 and K_1 , than that of T/P-J1-J2 track, so that satellites along T/PN-J1N track is expected to capture the internal tidal signal well.

The ADCP observations were used for the detailed analysis of slope internal tides. The data showed fairly strong internal wave continuum where the energy spectra of the internal tides are higher than those in the GM reference spectra by roughly about 2-3 times. Significant spectral peaks are observed at semidiurnal (M_2 , S_2) and diurnal frequencies (K_1 , O_1). The vertical structure of tidal ellipses for different constituents and EOF modes reveal the dominance of first mode vertical structure for semidiurnal and diurnal bands. The higher modes are also found to be significant in diurnal IT. We identified a number of possible generation sites of internal tides across the mooring location, including the deep region and the shelf edge. The mooring location is found to be more favorable for the generation of diurnal IT than semidiurnal. Strong diurnal IT is triggered even by weak diurnal barotropic forcing in the location (Fig. 6). The significant higher mode diurnal IT (Table 3) also shows that the mooring location might be favorable for the generation of diurnal IT.

Slope and shelf internal tides off Jaigarh show seasonality but not in a similar way. On the shelf, internal tides are weak during March-April time, which are attributed to the weak stratification on the shelf during pre-monsoon time. However, on the slope, during the same period, the water column is well stratified (Fig. 9) and IT is also found to be strong. Even though the barotropic forcing over the shelf is three times larger than that on the slope, internal tides are weak on the shelf during this period. The generation of internal tide on the shelf is greatly controlled by the background stratification. During SW monsoon time, stratification on the shelf

increased considerably. This causes occasional intensification internal tides on the seabed with a clear upward energy propagation. On the slope region, the stratification remains more or less consistent over the period of observation. Thereby, IT on the slope remains strong during all seasons of the observation period. The deep permanent pycnocline also may be important in the generation of internal tides in the region, which persists all through the year without any seasonal variation (Gerkema et al., 2004). Another aspect is the part of internal tides propagating shoreward from the slope. The present observations show that the energy of internal tides is weak on the shelf and strong on the slope during the March-April period, which is consistent with the stratification in these regions during this period. This is possible if a part of internal tide propagating from the slope towards shore gets dissipated before reaching the location of shelf mooring due to the well-mixed state of shelf water, probably inhibiting their propagation. The present work is not conclusive on this aspect. We intend to carry out numerical modeling to understand the propagation of IT on the central shelf and slope off the west coast of India.

Acknowledgments. The funding for ADCP program was provided by the Council of Scientific and Industrial Research (CSIR) and Indian National Center for Ocean Information Services (INCOIS), Ministry of Earth Sciences. The first author thanks University Grants Commission (UGC) for his research fellowship. We thank Fernando Vijayan, G.S. Michael, S.T. Khalap, Yogesh Agarawadekar, C. Santhosh, M.K Amey and Ashok Kankonkar of the mooring group of the institute for their efforts for the deployment and maintenance of the ADCPs on the continental shelf and slope off the Indian coasts. Altimetry data used in the present study were developed, validated, and distributed by the CTOH/LEGOS, France. We thank CTOH for making available satellite altimeter data through AVISO website (<http://ctoh.legos.obs-mip.fr/products/coastal-products/coastal-products-1/tidal-constants/nindian/>) and Laurent Testut for providing suggestions. Thanks to Florent Lyard and his group for making available results of FES 2012 (<http://www.aviso.altimetry.fr/en/products/global-tide-fes.html>). The first author thanks Ilker Fer, D' Asaro, A.L. New, D. Shankar, and A.G Nidheesh for providing some suggestions on the work. Amol Prakash and Arnab Mukherjee provided their wavelet codes. This is NIO Contribution No. xxxxx.

References

- Alford, M.H., 2003. Redistribution of energy available for ocean mixing by long-range propagation of internal waves. *Nature* 423, 159–162. doi:10.1038/nature01628.
- Alford, M.H., Gregg, M.C., Zervakis, V., Kontoyiannis, H., 2012. Internal wave measurements on the cycladic plateau of the aegean sea. *J. Geophys. Res.* 117. doi:10.1029/2011jc007488.
- Amol, P., Shankar, D., Aparna, S.G., Shenoi, S.S.C., Fernando, V., Shetye, S.R., Mukherjee, A., Agarvadekar, Y., Khalap, S., Satelkar, N.P., 2012. Observational evidence from direct current measurements for propagation of remotely forced waves on the shelf off the west coast of india. *J. Geophys. Res.* 117. doi:10.1029/2011jc007606.
- Azevedo, A., Da Silva, J., New, A., 2006. On the generation and propagation of internal solitary waves in the southern bay of biscay. *Deep Sea Research Part I: Oceanographic Research Papers* 53, 927–941. doi:10.1016/j.dsr.2006.01.013.
- Baines, P.G., 1982. On internal tide generation models. *Deep Sea Research Part A. Oceanographic Research Papers* 29, 307–338. doi:10.1016/0198-0149(82)90098-X.
- Baines, P.G., 1986. Internal tides, internal waves and near-inertial motions. *Baroclinic processes on continental shelves* , 19–31doi:10.1029/CO003p0019.
- Becker, J.J., Sandwell, D.T., Smith, W.H.F., Braud, J., Binder, B., Depner, J., Fabre, D., Factor, J., Ingalls, S., Kim, S.H., Ladner, R., Marks, K., Nelson, S., Pharaoh, A., Trimmer, R., Rosenberg, J.V., Wallace, G., Weatherall, P., 2009. Global bathymetry and elevation data at 30 arc seconds resolution: SRTM30_PLUS. *Marine Geodesy* 32, 355–371. doi:10.1080/01490410903297766.
- Bell, C., Vassie, J., Woodworth, P., 1999. Pol/psmsl tidal analysis software kit 2000 (task-2000). Permanent Service for Mean Sea Level, CCMS Proudman Oceanographic Laboratory, Bidston Observatory, Birkenhead, UK 20.

- Carrère, L., Lyard, F., Cancet, M., Guillot, A., Roblou, L., 2012. Fes2012: A new global tidal model taking advantage of nearly 20 years of altimetry, in: Proceedings of meeting.
- Chatterjee, A., Shankar, D., McCreary, J., Vinayachandran, P.N., 2013. Yanai waves in the western equatorial indian ocean. *J. Geophys. Res.* 118, 1556–1570. doi:10.1002/jgrc.20121.
- Chelton, D.B., Deszoeke, R.A., Schlax, M.G., El Naggar, K., Siwertz, N., 1998. Geographical variability of the first baroclinic rossby radius of deformation. *Journal of Physical Oceanography* 28, 433–460. doi:10.1175/1520-0485(1998)028<0433:GVOTFB>2.0.CO;2.
- Chen, G., Xue, H., Wang, D., Xie, Q., 2013. Observed near-inertial kinetic energy in the northwestern south china sea. *J. Geophys. Res.* 118, 4965–4977. doi:10.1002/jgrc.20371.
- Colosi, J.A., Beardsley, R.C., Lynch, J.F., Gawarkiewicz, G., Chiu, C.S., Scotti, A., 2001. Observations of nonlinear internal waves on the outer new england continental shelf during the summer shelfbreak primer study. *J. Geophys. Res.* 106, 9587. doi:10.1029/2000jc900124.
- Da Silva, J.C.B., New, A.L., Magalhaes, J.M., 2009. Internal solitary waves in the mozambique channel: Observations and interpretation. *J. Geophys. Res.* (1978–2012) 114. doi:10.1029/2008JC005125.
- D’Asaro, E.A., 1985. The energy flux from the wind to near-inertial motions in the surface mixed layer. *Journal of Physical Oceanography* 15, 1043–1059. doi:10.1175/1520-0485(1985)015<1043:TEFFTW>2.0.CO;2.
- Duda, T.F., Lynch, J.F., Irish, J.D., Beardsley, R.C., Ramp, S.R., Chiu, C.S., Tang, T.Y., Yang, Y.J., 2004. Internal tide and nonlinear internal wave behavior at the continental slope in the northern south china sea. *Oceanic Engineering, IEEE Journal of* 29, 1105–1130. doi:10.1109/JOE.2004.836998.
- Egbert, G.D., Erofeeva, S.Y., 2002. Efficient inverse modeling of barotropic ocean tides. *Journal of Atmospheric and Oceanic Technology* 19, 183–204. doi:10.1175/1520-0426(2002)019<0183:EIMOBO>2.0.CO;2.

- Garrett, C., Kunze, E., 2007. Internal tide generation in the deep ocean. *Annu. Rev. Fluid Mech.* 39, 57–87. doi:10.1146/annurev.fluid.39.050905.110227.
- Gerkema, T., Lam, F.P.A., Maas, L.R., 2004. Internal tides in the bay of biscay: conversion rates and seasonal effects. *Deep Sea Research Part II: Topical Studies in Oceanography* 51, 2995–3008. doi:10.1016/j.dsr2.2004.09.012.
- Gerkema, T., Maas, L.R., van Haren, H., 2013. A note on the role of mean flows in doppler-shifted frequencies. *Journal of Physical Oceanography* 43, 432–441. doi:10.1175/JPO-D-12-090.1.
- Gonella, J., 1972. A rotary-component method for analysing meteorological and oceanographic vector time series, in: *Deep Sea Research and Oceanographic Abstracts*, Elsevier. pp. 833–846. doi:10.1016/0011-7471(72)90002-2.
- Kelly, S.M., Nash, J.D., 2010. Internal-tide generation and destruction by shoaling internal tides. *Geophysical Research Letters* 37. doi:10.1175/1520-0485(1985)015<0544:NIWPIG>2.0.CO;2.
- Klymak, J.M., Alford, M.H., Pinkel, R., Lien, R.C., Yang, Y.J., Tang, T.Y., 2011. The breaking and scattering of the internal tide on a continental slope. *Journal of Physical Oceanography* 41, 926–945. doi:10.1175/2010JPO4500.1.
- Kumar, P.V.H., Lekshmi, S., Jagadeesh, P., Anilkumar, K., Krishnakumar, G.V., Rao, A.D., 2010. Internal tides in the coastal waters of ne arabian sea: observations and simulations. *Marine Geodesy* 33, 232–244. doi:10.1080/01490419.2010.493494.
- Kundu, P.K., Cohen, L.M., 1990. *Fluid mechanics*. Academic, Calif .
- Kunze, E., 1985. Near-inertial wave propagation in geostrophic shear. *Journal of Physical Oceanography* 15, 544–565. doi:10.1175/1520-0485(1985)015<0544:NIWPIG>2.0.CO;2.
- Lamb, K.G., 2014. Internal wave breaking and dissipation mechanisms on the continental slope/shelf. *Annual Review of Fluid Mechanics* 46, 231–254. doi:10.1146/annurev-fluid-011212-140701.

- Lee, H.I., Wang, Y.H., Yang, Y., Wang, D.P., 2012. Temporal variability of internal tides in the northeast south china sea. *J. Geophys. Res.* (1978–2012) 117. doi:10.1029/2011JC007518.
- Levine, M.D., Padman, L., Muench, R.D., Morison, J.H., 1997. Internal waves and tides in the western weddell sea: Observations from ice station weddell. *J. Geophys. Res.* (1978–2012) 102, 1073–1089. doi:10.1029/96jc03013.
- Lien, R.C., Sanford, T.B., Jan, S., Chang, M.H., Ma, B.B., 2013. Internal tides on the east china sea continental slope. *Journal of Marine Research* 71, 151–185. doi:10.1357/002224013807343461.
- Magalhaes, J., da Silva, J., 2012. Sar observations of internal solitary waves generated at the estremadura promontory off the west iberian coast. *Deep Sea Research Part I: Oceanographic Research Papers* 69, 12–24. doi:10.1016/j.dsr.2012.06.002.
- Maraldi, C., Lyard, F., Testut, L., Coleman, R., 2011. Energetics of internal tides around the kerguelen plateau from modeling and altimetry. *J. Geophys. Res.* (1978–2012) 116. doi:10.1029/2010JC006515.
- Merrifield, M.A., Holloway, P.E., 2002. Model estimates of m2 internal tide energetics at the hawaiian ridge. *Journal of Geophysical Research: Oceans* (1978–2012) 107, 5–1. doi:10.1029/2001jc000996.
- Merrifield, M.A., Holloway, P.E., Johnston, T., 2001. The generation of internal tides at the hawaiian ridge. *Geophysical Research Letters* 28, 559–562. doi:10.1029/2000GL011749.
- Muacho, S., da Silva, J., Brotas, V., Oliveira, P., Magalhaes, J., 2014. Chlorophyll enhancement in the central region of the bay of biscay as a result of internal tidal wave interaction. *Journal of Marine Systems* 136, 22–30. doi:10.1016/j.jmarsys.2015.04.007.
- Mukherjee, A., Shankar, D., Aparna, S.G., Amol, P., Fernando, V., Fernandes, R., Khalap, S., Narayan, S., Agarvadekar, Y., Gaonkar, M., et al., 2013. Near-inertial currents off the east coast of india. *Continental Shelf Research* 55, 29–39. doi:10.1016/j.csr.2013.01.007.

- Müller, P., Olbers, D.J., Willebrand, J., 1978. The iwex spectrum. *J. Geophys. Res.* (1978–2012) 83, 479–500. doi:10.1029/JC083iC01p00479.
- Munk, W., 1981. Internal waves and small-scale processes. *Evolution of physical oceanography* , 264–291.
- Munk, W., Wunsch, C., 1998. Abyssal recipes ii: energetics of tidal and wind mixing. *Deep Sea Research Part I: Oceanographic Research Papers* 45, 1977–2010. doi:10.1016/S0967-0637(98)00070-3.
- Murphy, A.H., 1988. Skill scores based on the mean square error and their relationships to the correlation coefficient. *Monthly weather review* 116, 2417–2424. doi:10.1175/1520-0493(1988)116<2417:SSBOTM>2.0.CO;2.
- Naqvi, S.W.A., 1991. Geographical extent of denitrification in the arabian sea in relation to some physical processes. *Oceanologica Acta* 14, 281–290.
- Nash, J., Shroyer, E., Kelly, S., Inall, M., Duda, T., Levine, M., Jones, N., Musgrave, R., 2012. Are any coastal internal tides predictable? *oceanography* 25, 80–95. doi:10.5670/oceanog.2012.44.
- Nash, J.D., Kunze, E., Toole, J.M., Schmitt, R.W., 2004. Internal tide reflection and turbulent mixing on the continental slope. *Journal of Physical Oceanography* 34, 1117–1134. doi:10.1175/1520-0485(2004)034<1117:ITRATM>2.0.CO;2.
- Petruncio, E.T., Rosenfeld, L.K., Paduan, J.D., 1998. Observations of the internal tide in monterey canyon. *Journal of Physical Oceanography* 28, 1873–1903. doi:10.1175/1520-0485(1998)028<1873:OOTITI>2.0.CO;2.
- Rao, A.D., Joshi, M., Ravichandran, M., 2008. Oceanic upwelling and downwelling processes in waters off the west coast of india. *Ocean Dynamics* 58, 213–226. doi:10.1007/s10236-008-0147-4.
- Ray, R.D., Cartwright, D.E., 2001. Estimates of internal tide energy fluxes from topex/poseidon altimetry: Central north pacific. *Geophysical Research Letters* 28, 1259–1262. doi:10.1029/2000GL012447.
- Shankar, D., Shenoi, S.S.C., Nayak, R.K., Vinayachandran, P.N., Nampoothiri, G., Almeida, A.M., Michael, G.S., Ramesh Kumar, M.R., Sundar, D., Sreejith, O.P., 2005. Hydrography of the eastern arabian sea dur-

- ing summer monsoon 2002. *Journal of earth system science* 114, 459–474. doi:10.1007/BF02702023.
- Shenoi, S.S.C., Antony, M.K., Sundar, D., 1988. Nature of the observed oscillatory flows in shelf waters of the western continental shelf of india. *Journal of Coastal Research* , 617–626.
- Shenoi, S.S.C., Shankar, D., Michael, G.S., Kurian, J., Varma, K.K., Kumar, M.R.R., Almeida, A.M., Unnikrishnan, A.S., Fernandes, W., Barreto, N., Gnanaseelan, C., Mathew, R., Praju, K.V., Mahale, V., 2005. Hydrography and water masses in the southeastern arabian sea during march–june 2003. *Journal of earth system science* 114, 475–491. doi:10.1007/BF02702024.
- Shetye, S.R., Gouveia, A.D., Shenoi, S.S.C., Michael, G.S., Sundar, D., Almeida, A.M., Santanam, K., 1991. The coastal current off western india during the northeast monsoon. *Deep Sea Research Part A. Oceanographic Research Papers* 38, 1517–1529. doi:10.1016/0198-0149(91)90087-V.
- Shetye, S.R., Gouveia, A.D., Shenoi, S.S.C., Sundar, D., Michael, G.S., Almeida, A.M., Santanam, K., 1990. Hydrography and circulation off the west coast of india during the southwest monsoon 1987. *Journal of Marine Research* 48, 359–378. doi:10.1357/002224090784988809.
- Subeesh, M.P., Unnikrishnan, A.S., Fernando, V., Agarwadekar, Y., Khalap, S.T., Satelkar, N.P., Shenoi, S.S.C., 2013. Observed tidal currents on the continental shelf off the west coast of india. *Continental Shelf Research* 69, 123–140. doi:10.1016/j.csr.2013.09.008.
- Unnikrishnan, A.S., Antony, M.K., 1990. On vertical velocity fluctuations and internal tides in an upwelling region off the west coast of india. *Estuarine, Coastal and Shelf Science* 31, 865–873. doi:10.1016/0272-7714(90)90088-9.
- Unnikrishnan, A.S., Shetye, S.R., Michael, G.S., 1999. Tidal propagation in the gulf of khambhat, bombay high, and surrounding areas. *Proceedings of the Indian Academy of Sciences-Earth and Planetary Sciences* 108, 155–177. doi:10.1007/BF02842329.

- Xu, Z., Yin, B., Hou, Y., Xu, Y., 2013. Variability of internal tides and near-inertial waves on the continental slope of the northwestern south china sea. *J. Geophys. Res.* 118, 197–211. doi:10.1029/2012JC008212.
- Zhao, Z., Alford, M.H., Girtton, J.B., 2012. Mapping low-mode internal tides from multisatellite altimetry. *Oceanography-Oceanography Society* 25, 42. doi:10.5670/oceanog.2012.40.

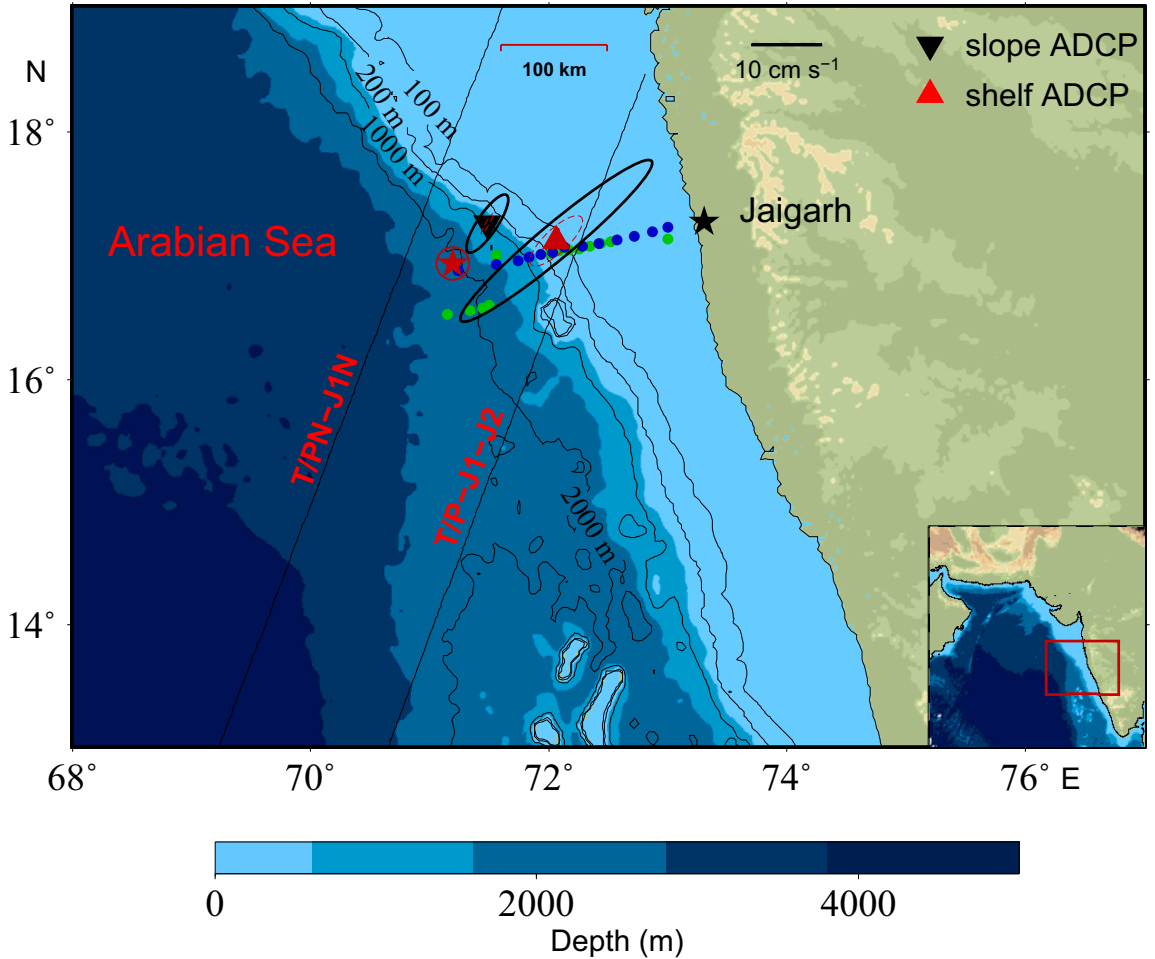


Figure 1: Locations of ADCP moorings. The two triangles are the locations of the shelf and slope ADCP moorings. Two lines are the satellite tracks, TOPEX/Poseidon-Jason-1-Jason-2 (T/P-J1-J2) and TOPEX/Poseidon-Jason-1 (T/PN-J1N), across the shelf-slope. Distance scale of satellite track is given at the top middle of the figure. The locations of 13 CTD casts across the slope-shelf region are shown. The green dots are the CTD casts along the shelf made during the February 2008 cruise and blue are the same made during April cruise. Barotropic M_2 (black bold line) and K_1 (red dotted line) ellipses for both shelf (Subeesh et al., 2013) and slope locations are shown. The amplitude scale bar for the ellipse is given in upper right. Two hourly CTD profiles were conducted from the deep location off Jaigarh (pentagram in red color) from 30th June to 10th July as a part of Arabian Sea Monsoon Experiment (ARMEX) which was carried out during summer monsoon 2002 (Shankar et al., 2005). The water depth of the location is 2250 m. Right inset map shows the west coast of India where the red box is the study area.

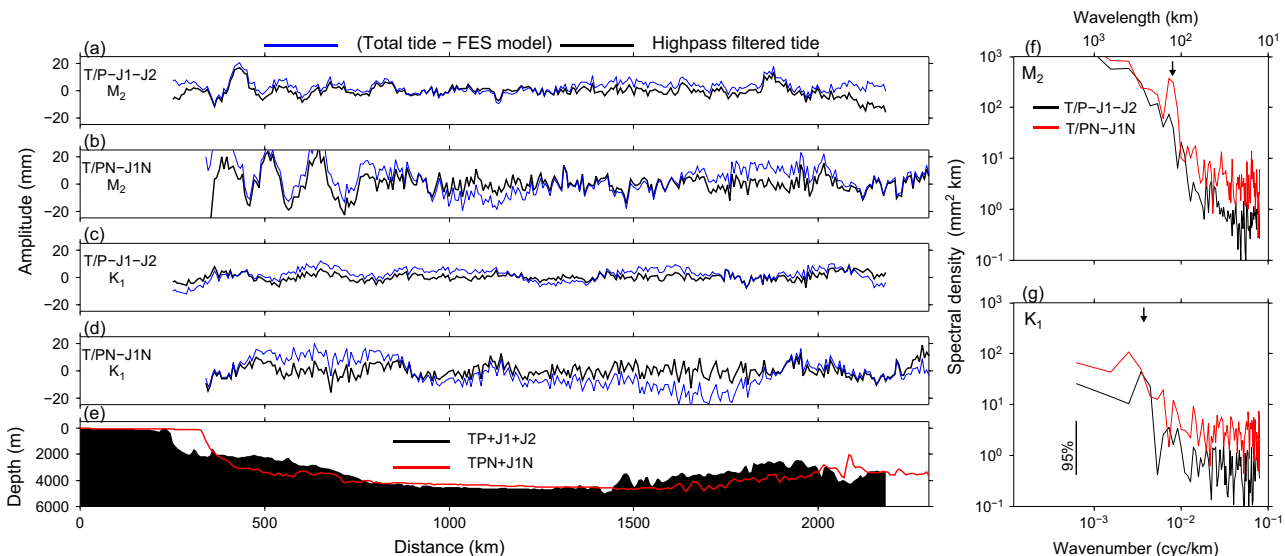


Figure 2: (a-d) M_2 and K_1 internal tides along the two ascending tracks, TOPEX/Poseidon-Jason-1-Jason-2 (T/P-J1-J2) and TOPEX/Poseidon-Jason-1 (T/PN-J1N) tracks. The black lines denote the internal tide obtained by the high-pass filtering (<1000 km) of along-track amplitude of the tidal constituents and blue lines denote the internal tide obtained by subtracting barotropic tidal constituents from along-track amplitude of tidal constituents. The barotropic tidal constituents were extracted from the global tidal model, FES 2012 output, for the two tracks. (e) Topography along the two tracks is shown. The black filled curve denotes the bottom topography along the T/P-J1-J2 track and red line is the topography along T/PN-J1N track. Along-track wavenumber spectra of the (f) M_2 and (g) K_1 are shown in the right panel. The two arrow marks in f and g denote the peaks in wavelengths at 125 km and 270 km respectively.

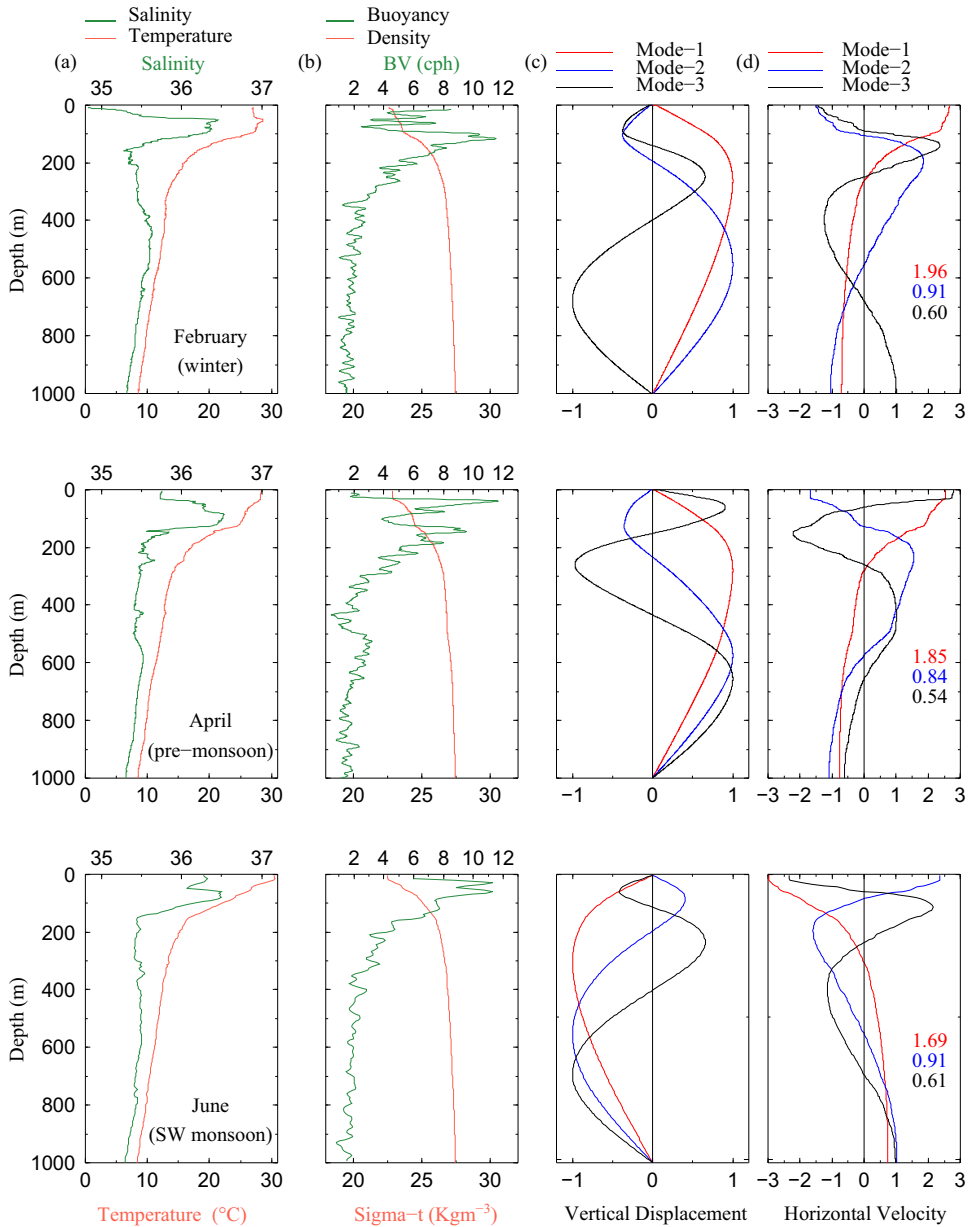


Figure 3: Hydrography profiles and the baroclinic normal modes for February, April and June at the slope location. (a) Temperature and salinity profiles (b) Density and buoyancy frequency (c) Normalised baroclinic modes for vertical displacement (d) Normalised baroclinic modes for horizontal velocity. Speed of each mode (m s^{-1}) is given in the figure.

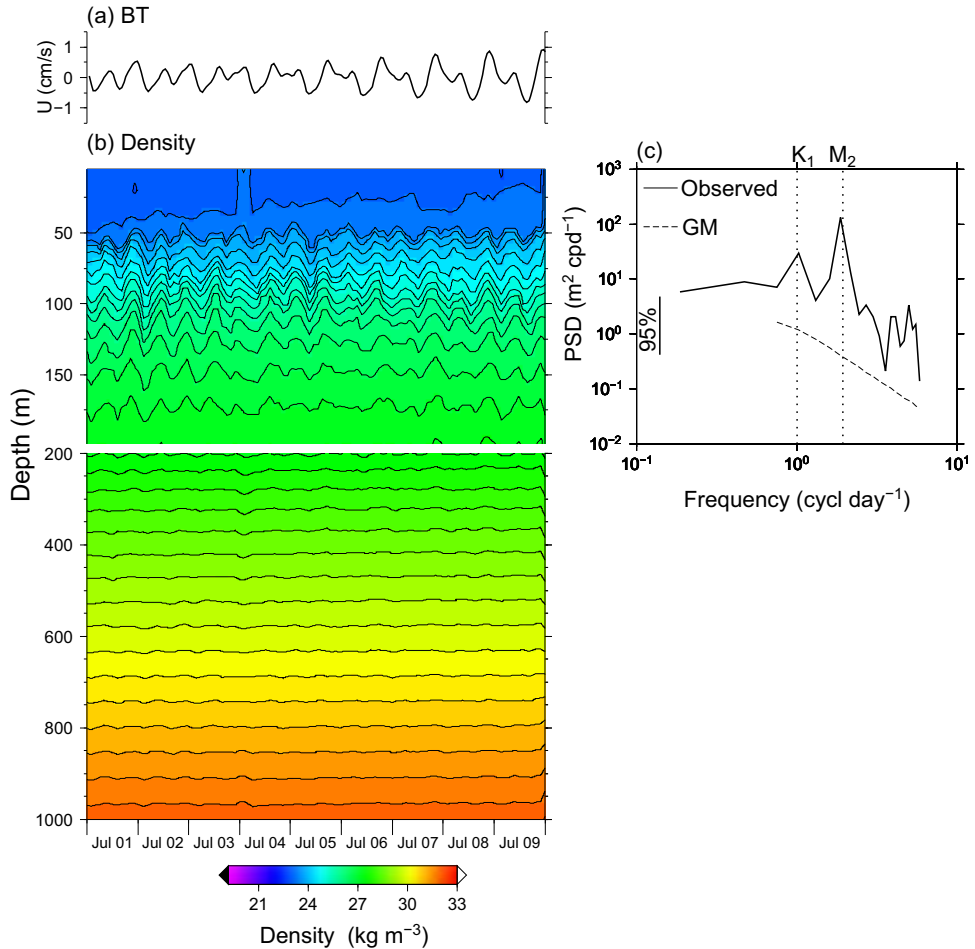


Figure 4: (a) Barotropic tidal current (BT) from OTPS output. (b) First 9-day density record in July 2002 computed from the temperature and salinity time series observation over the deep location off Jaigarh (shown in Fig. 1). (c) Power spectra of isopycnal displacement at 100 m. The dotted curve denotes the Garrett-Munk spectrum for the vertical displacement based on $N=2$ cph.

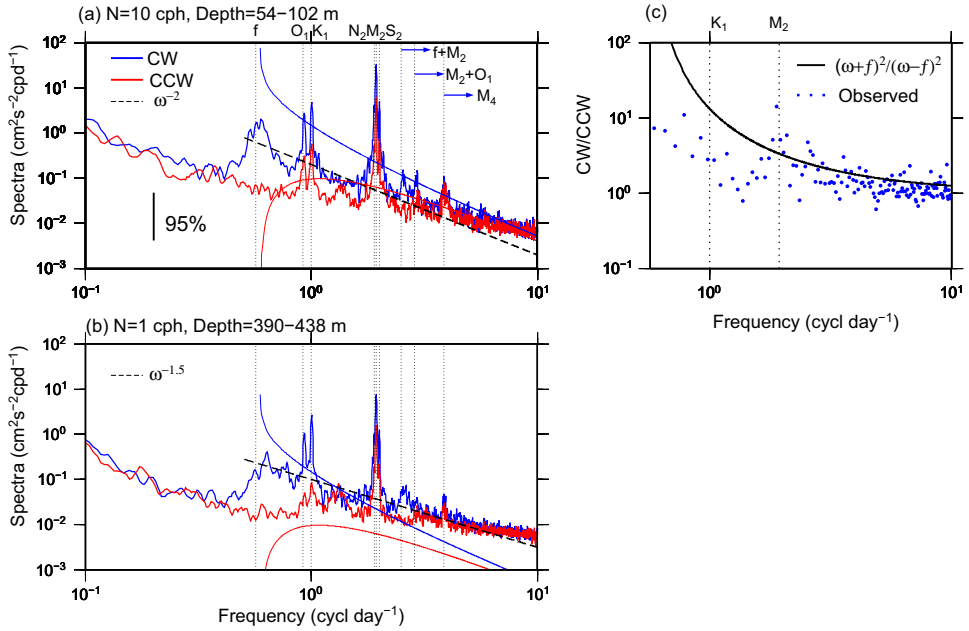


Figure 5: Rotary spectra of baroclinic currents. (a) Vertically averaged spectra for the upper water column (54-102 m). (b) same as (a) but for the water column of 390-438 m depth. The curves represent Garrett-Munk clockwise (blue) and counterclockwise (red) spectra. The GM spectra was calculated using $N=10$ cph for upper water column and 1 cph for the water column at 390-438 m depth. The dotted lines indicate ω^{-2} and $\omega^{-1.5}$, where ω is the frequency. The 95% confidence level is also shown. (c) ratio of vertically averaged clockwise and counterclockwise spectra (blue dots). The black line is the theoretical ratio (Müller et al., 1978).

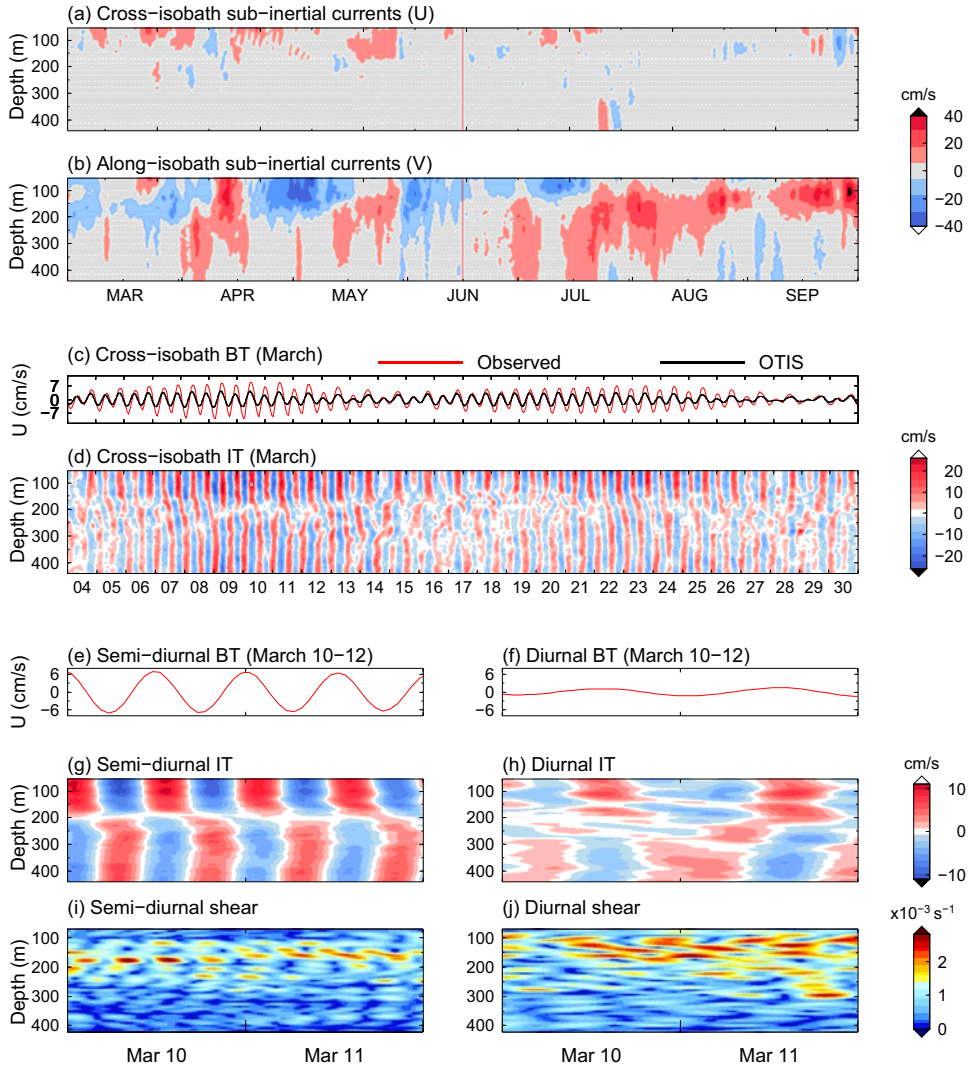


Figure 6: Time series of (a) Cross-isobath sub-inertial currents (b) Along-isobath sub-inertial currents. (c) Result of harmonic analysis of cross-isobath barotropic current along with the OTIS output for the month of March (d) the corresponding band passed IT. The harmonic analysis was carried out on the cross-isobath barotropic currents by keeping semidiurnal and diurnal constituents separately. (e-j) A two-day BT and IT are zoomed for both semidiurnal and diurnal bands and the time evolution of 8 m vertical shear (s^{-1}) corresponding to both bands are shown.

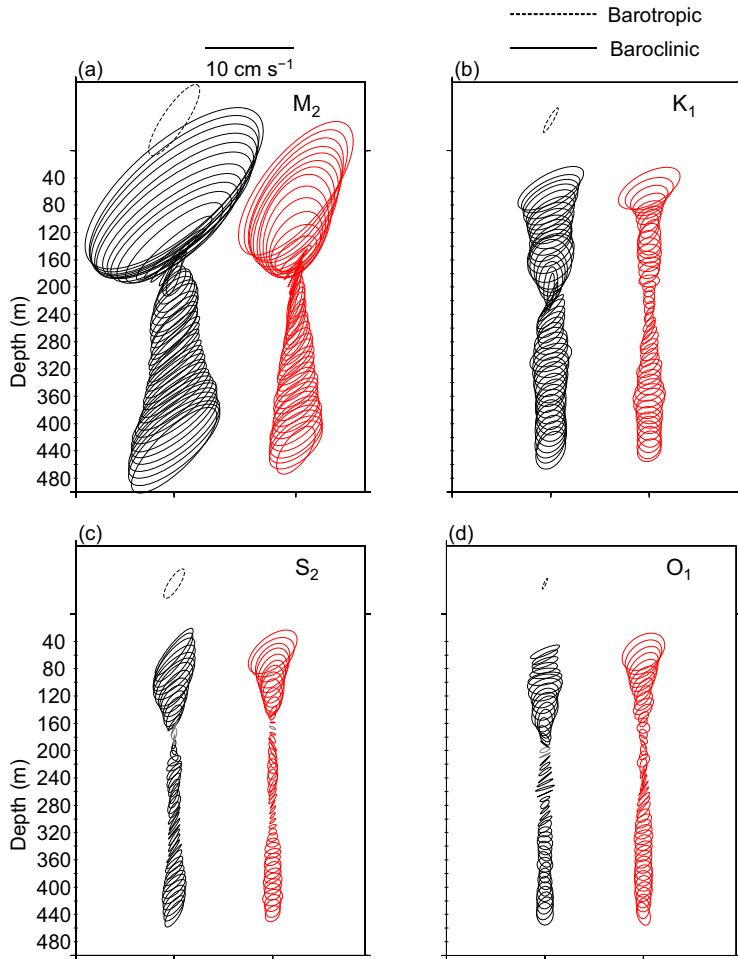


Figure 7: Baroclinic (bold line) and barotropic (dotted line) tidal ellipses of (a) M₂, (b) K₁, (c) S₂, and (d) O₁. Baroclinic tidal ellipses were constructed for March-May (black line) and June-August (red line) periods. Barotropic ellipses were constructed for the entire period of observation. The scale is shown on the top. All ellipses rotate in clockwise direction.

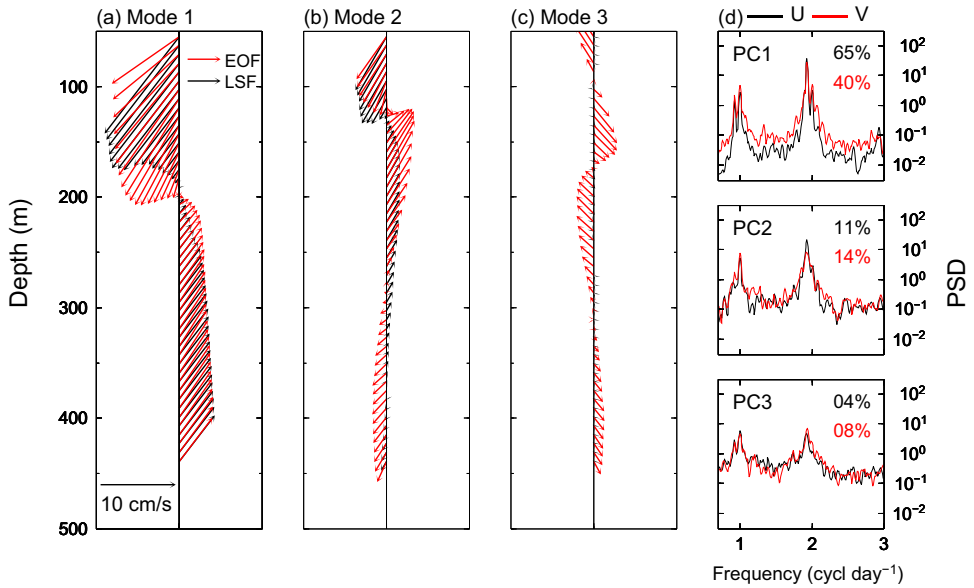


Figure 8: The vectors (red color) are derived from the cross-isobath (U) and along-isobath (V) EOF modes. First three EOF modes are shown here. The black color vectors indicate the least square fits (LSF) (equation 9) for the first three EOF modes. (d) power spectra of the principal component of each EOF mode of U (black) and V (red). The percentage of variance contributed by each mode is shown.

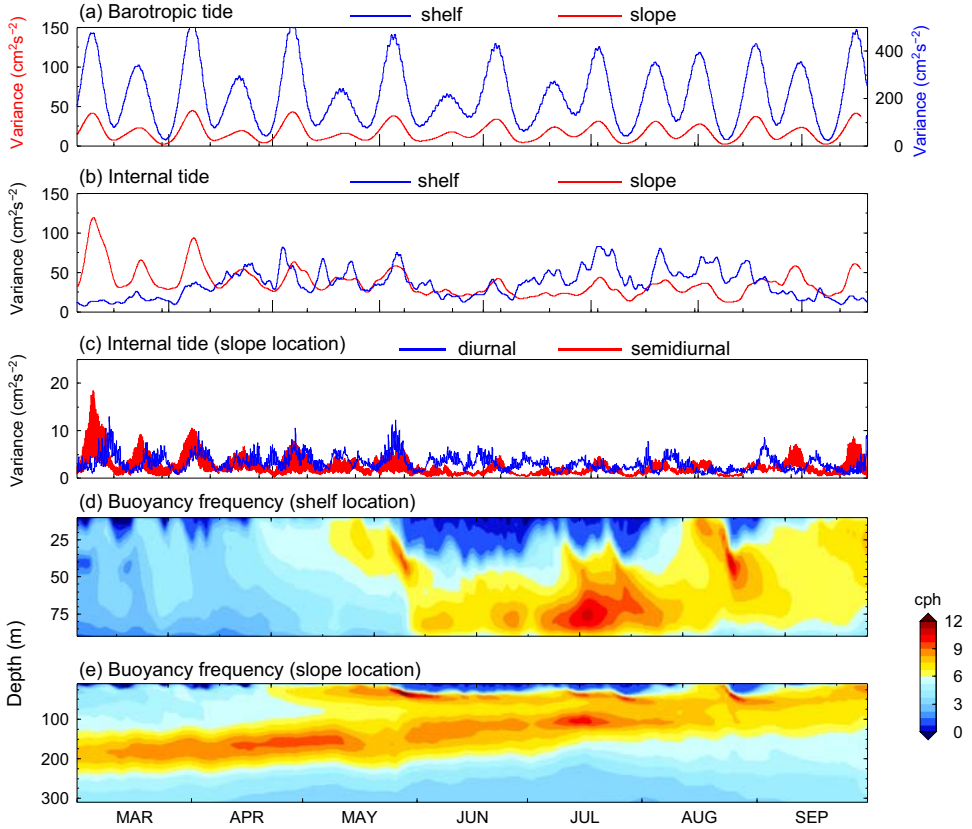


Figure 9: (a) Time series of variance of barotropic tidal currents ($u^2 + v^2$) for shelf and slope locations. A running 3-day averaging was applied on the variance. The scale for shelf BT is given on the right axis and that of slope BT is given on the left axis. (b) Time series of IT variance. Variance was vertically averaged and a running average over 3 days applied before plotting. (c) Time series of semidiurnal and diurnal IT variance on the slope location. The variance was vertically averaged but not smoothed in time. (d-e) The buoyancy frequency distribution during the ADCP observation period near the mooring locations, on the shelf and slope, computed using hydrography from MOM4p1 model output (Chatterjee et al., 2013). For the slope location, only upper 300 m values are shown.

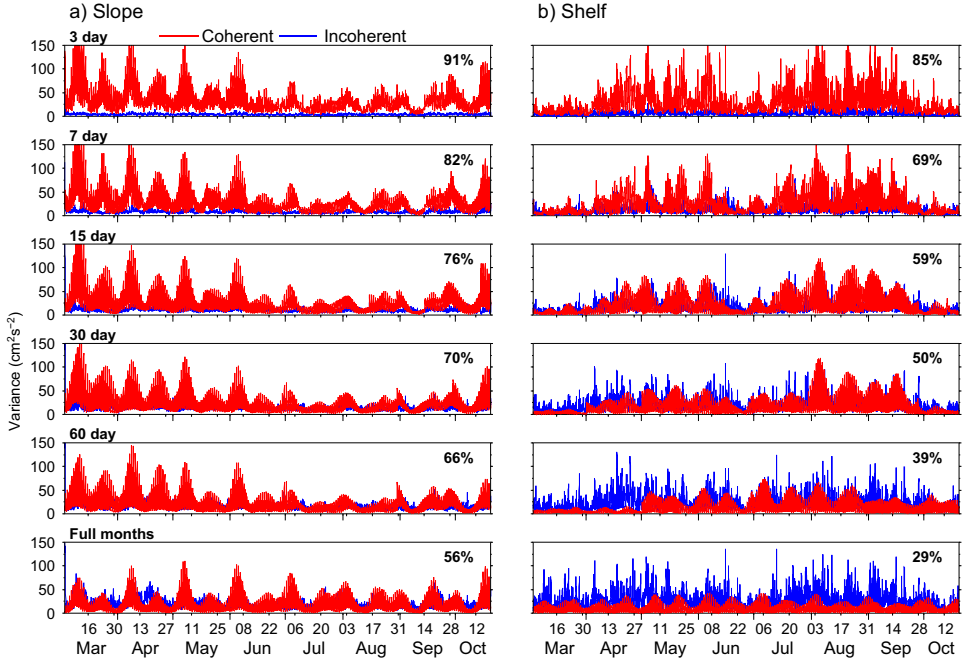


Figure 10: Time series of coherent and incoherent IT variance ($u^2 + v^2$) for the (a) slope and (b) shelf locations. Harmonic analysis over different time span was carried out on the broad band (6-30 hrs) internal tide and the time series were generated. The variance of the regenerated harmonic analysis ($U_H^2 + V_H^2$) (red) and that of the residual ($U_R^2 + V_R^2$) (blue) are shown. The variance was averaged over depth. The time span taken for harmonic analysis is indicated in each panel. Skill score (equation 10) was calculated for each harmonic analysis and predictability was determined. The percentage of predictability is also shown in each panel.

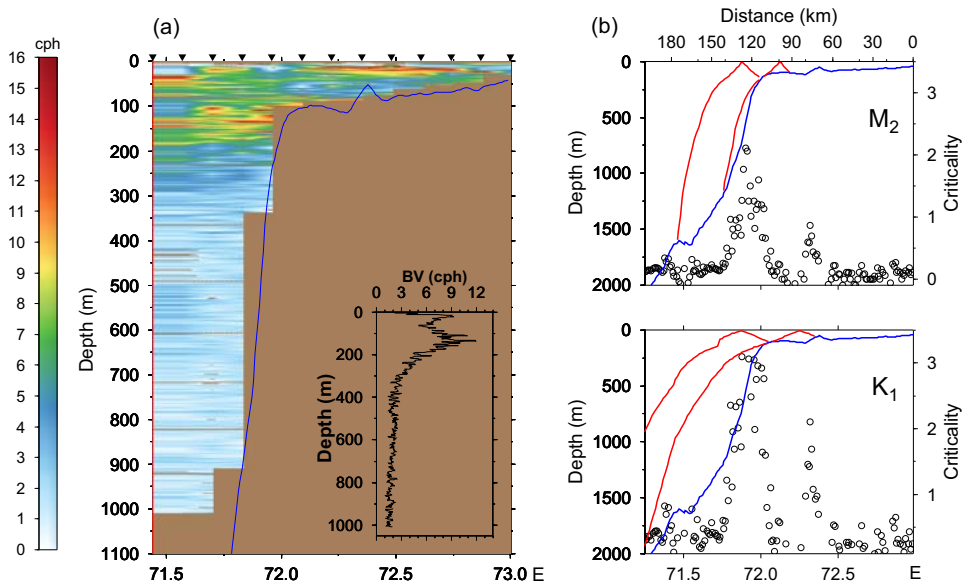


Figure 11: (a) Buoyancy frequency from 13 CTD casts during April 2008 (the transect shown by green dots in Fig. 1), across the moorings. The triangles are the locations of CTD measurements across the shelf. Bottom topography along the cruise observations is also marked in blue line. The inset map shows the spatially averaged buoyancy frequency. (b) The black circles denote the criticality parameter (the ratio between bottom slope and characteristic slope) of M_2 and K_1 along the cruise track. Characteristic slopes were computed using the buoyancy frequency values near the bottom. Bottom slope was calculated using SRTM30_PLUS bathymetry. M_2 and K_1 internal wave characteristics emanating from shelf edge, where the bottom slope is nearly equal to the characteristic slope, are shown. Distance from the location of CTD cast nearest to the coast is shown in the north axis.

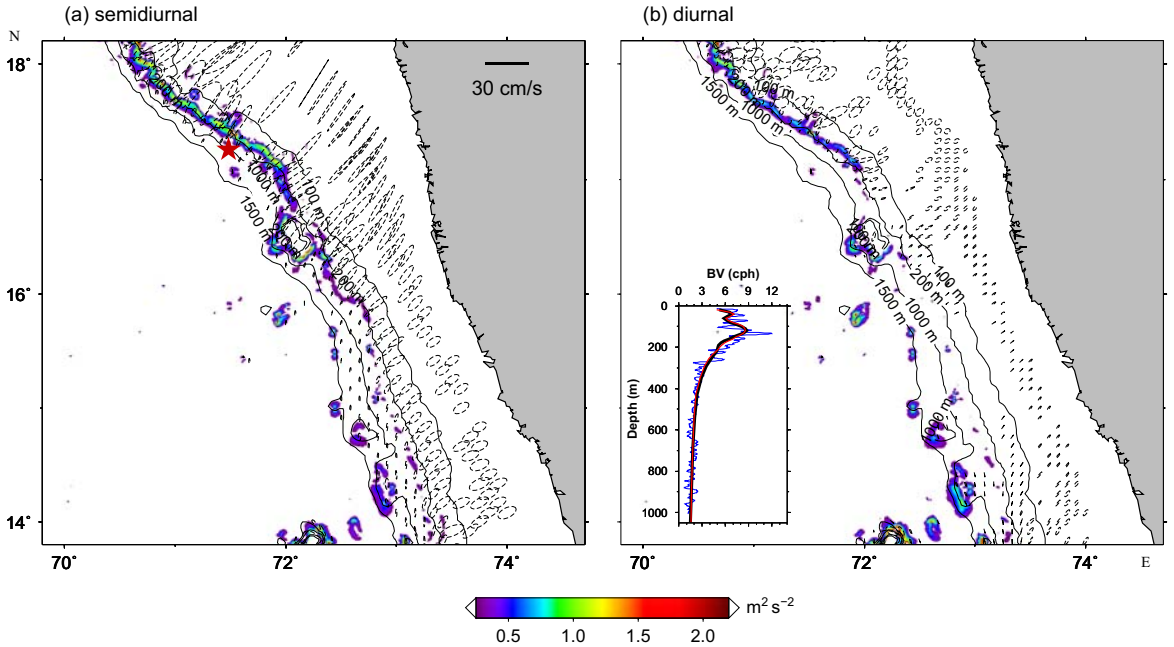


Figure 12: Spatial distribution of maximum depth-integrated (a) semidiurnal and (b) diurnal barotropic body force (equation 12) for April. The vertical profile of spatially-averaged monthly climatology of buoyancy frequency for April, used for the body force calculation, is shown in the inset map (black bold line). The vertical profile of buoyancy frequency from monthly climatology (red line) and CTD observation (blue line) on the slope for April are also shown. The blue line denotes the stratification on the slope obtained from the in situ CTD observation. M_2 and K_1 tidal ellipses are shown with the semidiurnal and diurnal body force. The red triangle denotes the location of slope ADCP mooring. 100, 200, 1000 and 1500 m depth contours are also shown.

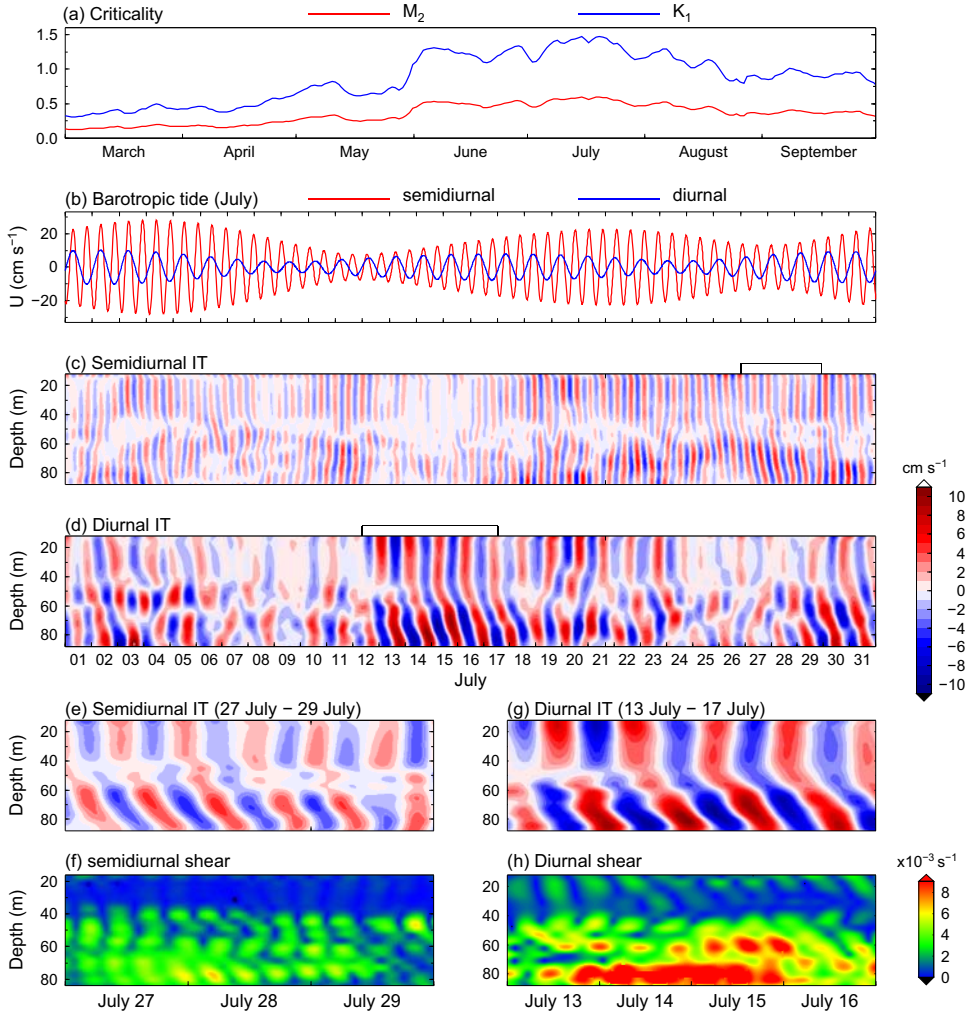


Figure 13: (a) The criticality parameter for M_2 and K_1 for the entire observation period. The characteristic slopes were estimated using the bottom buoyancy frequency obtained from the temperature and salinity values of MOM4p1 model output (Chatterjee et al., 2013). (b-d) The BT and IT for semidiurnal and diurnal band are zoomed for July. We further zoomed semidiurnal and diurnal IT (The marked portion of (c) and (d)) in (e) and (g) and the evolution of 8 m vertical shear (s^{-1}) for the same period is shown in (f) and (h).

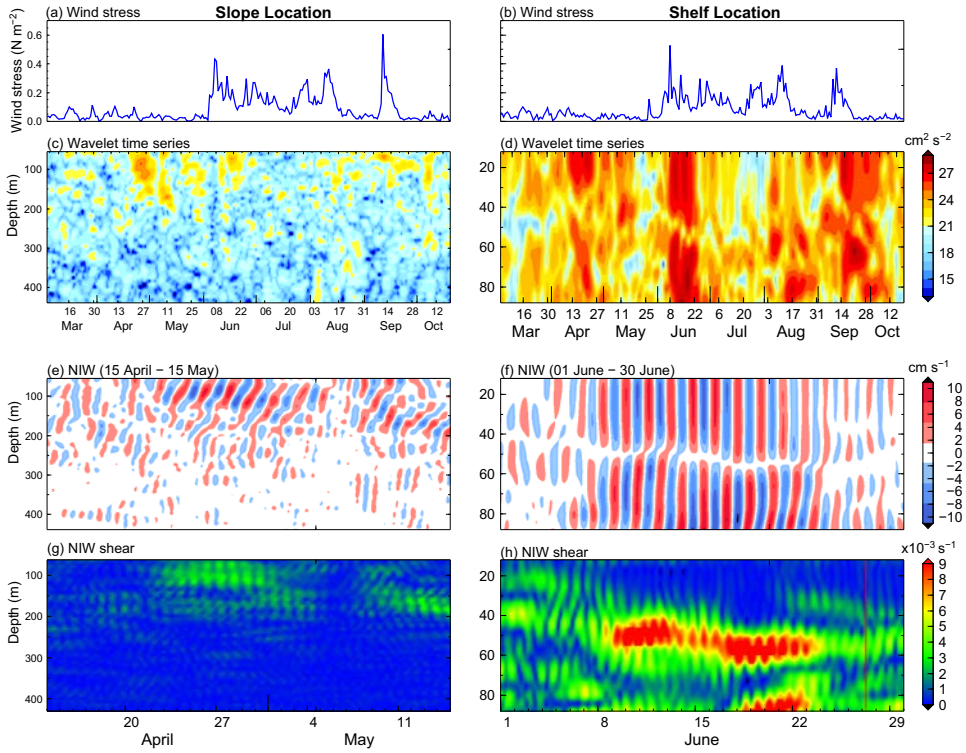


Figure 14: (a-b) 4-day high pass wind stress (QuikSCAT) over the slope and shelf locations is shown during the period of observation. (c-d) The band averaged ($0.85-1.15f$, where f is the Coriolis frequency) wavelet spectra of NIW. (e-f) Time series of cross-isobath component of NIW. (g-h) 8 m vertical shear evolution of NIW for the same period. Two strong NIW events observed during 15 April- 15 May (at slope) and 01 June- 30 June (at shelf) are considered for Fig. e,f,g and h.

Table 1: Phase speed (C_p), Group speed (C_g) and Wavelength (λ) of the first three modes of M_2 , S_2 , K_1 and O_1 internal tides on the slope location. Normal modes were computed from the CTD data of February, April and June.

		M_2			S_2			K_1			O_1		
	Mode	C_p	C_g	λ	C_p	C_g	λ	C_p	C_g	λ	C_p	C_g	λ
		m/s	m/s	km	m/s	m/s	km	m/s	m/s	km	m/s	m/s	km
Feb	1	2.0	1.8	91.1	2.0	1.8	87.8	2.3	1.6	203.5	2.4	1.5	228.4
	2	0.9	0.9	43.0	0.9	0.8	41.4	1.1	0.7	096.0	1.1	0.7	107.7
	3	0.6	0.5	28.0	0.6	0.5	27.0	0.7	0.4	062.6	0.7	0.4	070.3
Apr	1	1.9	1.7	86.9	1.9	1.7	83.7	2.2	1.5	194.1	2.3	1.4	217.9
	2	0.8	0.8	39.2	0.8	0.8	37.8	1.0	0.6	087.6	1.0	0.6	098.4
	3	0.5	0.5	25.2	0.5	0.5	24.3	0.6	0.4	056.3	0.6	0.4	063.2
Jun	1	1.8	1.6	79.0	1.8	1.6	76.1	2.0	1.4	176.4	2.1	1.3	198.0
	2	1.0	0.9	42.5	0.9	0.9	50.0	1.1	0.8	095.0	1.1	0.7	106.6
	3	0.6	0.6	28.5	0.6	0.6	27.4	0.7	0.5	063.6	0.8	0.5	071.4

Table 2: Semimajor and semiminor axes, inclination and Greenwich phase of barotropic tidal ellipses on the slope location. The entire observation period was taken to carry out the harmonic analysis.

	Semimajor (cm s ⁻¹)	Semiminor (cm s ⁻¹)	Inclination (deg)	Phase (deg)
M ₂	4.8	1.4	56	324.1
S ₂	2.0	0.6	57	348.8
K ₁	1.6	0.3	60	051.1
O ₁	0.6	0.1	66	038.1

Table 3: The percentage EOF variance for the semidiurnal and diurnal IT on the slope location.

	Semidiurnal		diurnal	
	Cross-isobath	Along-isobath	Cross-isobath	Along-isobath
	(%)	(%)	(%)	(%)
Mode 1	78	55	45	37
Mode 2	10	14	13	11
Mode 3	02	07	08	10
Mode 4	01	05	06	06